

# A reduced-order, single-bubble cavitation model with applications to therapeutic ultrasound

Wayne Kreider,<sup>a)</sup> Lawrence A. Crum, and Michael R. Bailey  
*Center for Industrial and Medical Ultrasound, Applied Physics Laboratory, University of Washington,  
1013 Northeast 40th Street, Seattle Washington 98105*

Oleg A. Sapozhnikov<sup>b)</sup>  
*Department of Acoustics, Physics Faculty, Moscow State University, Leninskie Gory, Moscow 119991, Russia*

(Received 13 December 2010; revised 17 June 2011; accepted 20 June 2011)

Cavitation often occurs in therapeutic applications of medical ultrasound such as shock-wave lithotripsy (SWL) and high-intensity focused ultrasound (HIFU). Because cavitation bubbles can affect an intended treatment, it is important to understand the dynamics of bubbles in this context. The relevant context includes very high acoustic pressures and frequencies as well as elevated temperatures. Relative to much of the prior research on cavitation and bubble dynamics, such conditions are unique. To address the relevant physics, a reduced-order model of a single, spherical bubble is proposed that incorporates phase change at the liquid-gas interface as well as heat and mass transport in both phases. Based on the energy lost during the inertial collapse and rebound of a millimeter-sized bubble, experimental observations were used to tune and test model predictions. In addition, benchmarks from the published literature were used to assess various aspects of model performance. Benchmark comparisons demonstrate that the model captures the basic physics of phase change and diffusive transport, while it is quantitatively sensitive to specific model assumptions and implementation details. Given its performance and numerical stability, the model can be used to explore bubble behaviors across a broad parameter space relevant to therapeutic ultrasound. © 2011 Acoustical Society of America. [DOI: 10.1121/1.3626158]

PACS number: 43.35.Ei [CCC]

Pages: 3511–3530

## I. INTRODUCTION

In medical ultrasound, cavitation and bubble dynamics are often important. In diagnostic applications, micron-sized bubbles can be injected into the bloodstream to reflect incident acoustic waves and enhance imaging contrast. To better understand how these bubbles interact with diagnostic ultrasound, the dynamics of shelled contrast-agent microbubbles have received much attention in the recent literature.<sup>1</sup> In addition, various therapeutic ultrasound applications that involve bubbles are being used and/or developed. While shock-wave lithotripsy (SWL) for renal stone comminution and high-intensity focused ultrasound (HIFU) for thermal tissue ablation are well known and are used clinically, other therapeutic applications include ultrasound-assisted drug delivery<sup>2</sup> and mechanical tissue fractionation.<sup>3</sup> Given the unique conditions that can be associated with therapeutic ultrasound (high acoustic pressures, megahertz frequencies, elevated temperatures), understanding the mechanics underlying the corresponding cavitation behaviors remains an active area of research.

For medical ultrasound, the relevant initial bubble sizes are on the order of microns or smaller. At medical frequencies and therapeutic excitation amplitudes on the order of

megapascals or tens of megapascals, such bubbles are expected to undergo large changes in size that involve inertial collapses and rebounds in addition to rapid condensation/evaporation at the bubble wall (i.e., the liquid-gas interface). Moreover, contrast-agent microbubbles will likely rupture their shells and become free gas bubbles at pressures above about 1 MPa.<sup>4</sup> Given that contrast-agent microbubbles are administered by injection into the bloodstream while endogenous cavitation nuclei typically exist in blood or other fluid spaces,<sup>5,6</sup> the fundamental physics of bubbles subjected to therapeutic ultrasound can be explored by considering the case of a single, free bubble in a liquid. Although a bubble within a blood vessel may not be “free” due to the viscoelastic stiffness of the vessel and surrounding tissue structures, investigation of such bubble-vessel interactions is a separate area of research<sup>7–9</sup> and is beyond the scope of the present work. Here we focus on understanding how heat and mass transport affect bubble motions in the context of high excitation pressures and/or elevated temperatures.

In surveying previous models used to simulate bubbles exposed to therapeutic ultrasound, we note that the dynamics of a single, spherical bubble were typically considered. For bubbles excited by a lithotripter shock wave, Church<sup>10</sup> and later Sapozhnikov *et al.*<sup>11</sup> modeled the diffusive transport of non-condensable gases, but neglected phase change at the bubble wall. Also for lithotripsy bubbles, Matula *et al.*<sup>12</sup> accounted for phase change and implemented a reduced-order model based on scaling principles to estimate heat and mass transport; however, the model was found to be quite sensitive to indeterminate “free” parameters that emerged

<sup>a)</sup>Author to whom correspondence should be addressed. Electronic mail: [wkreider@uw.edu](mailto:wkreider@uw.edu).

<sup>b)</sup>Also at: Center for Industrial and Medical Ultrasound, Applied Physics Laboratory, University of Washington, 1013 Northeast 40th Street, Seattle WA 98105.

from the scaling. For HIFU bubbles, models have either neglected phase change at the bubble wall<sup>13,14</sup> or considered very low acoustic forcing amplitudes ( $\sim 1$  bar) in conjunction with phase change and associated transport behaviors.<sup>15</sup> The limitation of this latter model in addressing only low excitation amplitudes highlights an important challenge: maintaining numerical stability through violent inertial collapses.

Although not explicitly applied to bubbles excited by therapeutic ultrasound, models that include the relevant transport behaviors have been developed to simulate the violent collapses of sonoluminescence bubbles.<sup>16,17</sup> As noted by Vuong and Szeri<sup>16</sup> and Preston,<sup>18</sup> numerical implementation of this type of direct model poses difficulties due to the very sharp spatial gradients that can occur. Overall, sonoluminescence models possess a high degree of complexity, which is needed to represent details of the gas dynamics that lead to light production in the end stages of a violent collapse. However, it is not clear that such small-scale complexity and the associated computational expense is warranted for the large-scale behaviors of interest here.

The goal of this effort is to develop a numerically stable, reduced-order model that accounts for phase change and diffusive transport in order to estimate the bubble's total energy. Because energy dissipation occurs primarily during violent inertial collapses, we focus on the model's ability to simulate a single collapse and rebound, which can be taken as a fundamental component of the bubble motion. The ensuing sections present the model as follows: first, the model and its numerical implementation are described in detail; then, experimental observations of the collapses and rebounds of lithotripsy bubbles<sup>19</sup> are used to tune two model parameters and assess model performance; next, the tuned model is benchmarked against results published in the literature; last, the model is used to explore how ambient temperature and vapor affect the collapses of bubbles excited by HIFU.

## II. MODEL

To begin description of the model, it is instructive to provide a brief overview. The model is formulated by first assuming spherical symmetry and enforcing the conservation of mass and momentum in the liquid. This Rayleigh-Plesset style approach yields an ordinary differential equation (ODE) for the bubble radius. The formulation is completed by calculating pressure in the gas phase as a time-dependent boundary condition for the aforementioned ODE. In this approach, pressure inside the bubble is calculated by enforcing an energy balance on the contents of the bubble and considering heat and mass transport at the liquid-gas interface (i.e., at the bubble "wall"). The energy associated with chemical reactions during a violent bubble collapse is relatively small<sup>20</sup> and is neglected here. In addition, mass diffusion associated with species created by chemical reactions is neglected.

Here, mass transport includes both the evaporation/condensation of vapor and the diffusion of non-condensable gases dissolved in the liquid. Inside the bubble, both mass and heat diffusion are modeled by assuming a uniform spatial distribution of thermodynamic variables everywhere

except within a boundary layer at the bubble wall. Assuming constant gradients in these boundary layers, transport is approximated using Fickian equations along with estimates of boundary-layer thicknesses based on scaling considerations. In the liquid, the spatial variation of temperature is addressed differently in two separate model variations. In the "scaling" model variation (SCL model), uniform liquid temperature is assumed everywhere outside of a boundary layer near the bubble wall and the aforementioned Fickian approach is utilized for calculating thermal conduction. In the other model variation (termed the "PZ model" here, after Plesset and Zwick's approach<sup>21</sup>), no such assumption is made. Rather, an approximate solution is utilized to account for thermal conduction in the presence of convective flow. For mass transport in the liquid, an approach fully analogous to that used in the PZ model is implemented for diffusion of dissolved gases.<sup>22</sup> The full model formulation is described in detail below.

### A. Radial dynamics

For spherically symmetric bubbles, modeling typically begins with the conservation equations for mass and momentum in the liquid. Combining these equations and spatially integrating over the radial coordinate  $r$  from the bubble radius  $R$  to infinity produces a single, second-order ODE for the bubble radius. This formulation is then completed by calculating a uniform gas pressure inside the bubble  $p_i$  as a function of the thermodynamic state of the bubble. Models formulated in this fashion are commonly termed Rayleigh-Plesset (RP) models. As discussed in detail by Lin *et al.*,<sup>23</sup> the assumption of uniform pressure inside the bubble produces accurate solutions even for violent bubble collapses. Simple RP models that assume liquid incompressibility and/or polytropic gas behavior are often used; however, to better capture the physics of inertial collapses, both liquid compressibility and a full energy balance of the gas phase are considered in this effort. Both the ODE for bubble motion and the method of calculating the gas pressure are described in the remainder of this section.

To account for liquid compressibility, various equations have been developed and used for studying bubble dynamics.<sup>24–29</sup> As shown by Prosperetti and Lezzi,<sup>30</sup> these equations all belong to a family of RP models that can be understood in the context of an asymptotic expansion in which the acoustic Mach number  $\dot{R}/c_0$  is the "small" parameter. Here,  $c_0$  is the speed of sound in the liquid at reference conditions far from the bubble, and the overdot indicates a time derivative. In this context, the Keller-Miksis<sup>29</sup> and Herring-Trilling<sup>27,28</sup> equations are first-order formulations, while the Gilmore equation contains additional second-order terms. Due in part to its explicit formulation in terms of liquid enthalpy at the bubble wall, the Gilmore equation has been found to perform remarkably well during inertial collapses.<sup>30</sup> Accordingly, the Gilmore equation is used here and is described in detail below. The formulation presented below follows that described by Sapozhnikov *et al.*<sup>11</sup>

In terms of enthalpy, the Gilmore equation<sup>26</sup> can be written as

$$\begin{aligned} & \left(1 - \frac{\dot{R}}{C}\right)R\ddot{R} + \frac{3}{2}\left(1 - \frac{\dot{R}}{3C}\right)\dot{R}^2 \\ & = \left(1 + \frac{\dot{R}}{C}\right)H + \left(1 - \frac{\dot{R}}{C}\right)\frac{R}{C}\dot{H}, \end{aligned} \quad (1)$$

where capital letters  $C$  and  $H$  denote the liquid sound speed and enthalpy evaluated at the bubble wall. Before defining these quantities explicitly, it is helpful to first specify an equation of state for the liquid. To this end, we define a modified form of the Tait equation to relate pressure  $p$  and density  $\rho$  in the liquid as follows:<sup>31</sup>

$$p = p_0 + \frac{1}{b\Gamma} \left[ \left( \frac{\rho}{\rho_0} \right)^\Gamma - 1 \right] \quad \text{where} \quad b = \frac{1}{\rho_0 c_0^2}. \quad (2)$$

In general,  $\Gamma$  and  $b$  are empirical constants, and the “0” subscripts denote liquid properties at a reference state that corresponds to static conditions in the ambient liquid. As noted above,  $b$  is defined in terms of the reference sound speed  $c_0$  in order to maintain consistency with the typical definition of sound speed. From data for water over a range of temperatures,  $\Gamma = 6.5$  is selected here.<sup>31</sup>

Now, enthalpy  $h$  and sound speed  $c$  can be defined throughout the liquid as

$$h = \int_{p_\infty}^p \frac{dp}{\rho} = \frac{c^2 - c_\infty^2}{\Gamma - 1}, \quad (3)$$

$$c^2 = \frac{dp}{d\rho} = \frac{\Gamma(p + B)}{\rho}, \quad (4)$$

where the “ $\infty$ ” subscripts denote values far from the bubble and  $B \equiv 1/(b\Gamma) - p_0$ .

To implement the model,  $c$  and  $h$  must be evaluated at the bubble wall. Such evaluations require determination of the pressure in the liquid at the wall  $p_w$ . Assuming that a uniform gas pressure inside the bubble  $p_i$  is known, the pressure in the liquid can be calculated by accounting for viscosity  $\mu$  and surface tension  $\sigma$ :

$$p_w = p_i - \frac{4\mu\dot{R}}{R} - \frac{2\sigma}{R}. \quad (5)$$

In this expression, the term with surface tension arises from Laplace’s relation<sup>32</sup> while the viscosity term is derived from the three-dimensional stress state of an incompressible liquid at the gas-liquid interface.<sup>33</sup> For practical implementation of the Gilmore model as written in Eq. (1) above, it is convenient to evaluate sound speed, enthalpy, and the time derivative of enthalpy at the bubble wall as follows:

$$H = \frac{(b\Gamma)^{-1/\Gamma}}{\rho_0} \frac{\Gamma}{\Gamma - 1} \left[ (p_w + B)^{(\Gamma-1)/\Gamma} - (p_0 + p_{ac} + B)^{(\Gamma-1)/\Gamma} \right], \quad (6)$$

$$\dot{H} = \frac{(b\Gamma)^{-1/\Gamma}}{\rho_0} \left[ (p_w + B)^{-1/\Gamma} \dot{p}_w - (p_0 + p_{ac} + B)^{-1/\Gamma} \dot{p}_{ac} \right], \quad (7)$$

$$C^2 = c_0^2 + (\Gamma - 1)H. \quad (8)$$

Note that in this formulation, enthalpy at the bubble wall is calculated with the understanding that the pressure at infinity is the sum of the reference pressure and the acoustic forcing (i.e.,  $p_\infty = p_0 + p_{ac}$ ). However, given the implicit assumption that the acoustic forcing is applied instantaneously around the bubble without specifying a source location, the physical sound speed far from the bubble is taken at the static reference state, i.e.,  $c_\infty = c_0$ . The above expressions are suitable for inclusion in a computer program and clearly illustrate that the acoustic forcing appears through its impact on the local enthalpy ( $H, \dot{H}$ ). Last, this formulation permits calculation of the pressure “radiated” from the bubble in the form of an outward traveling spherical wave. Evaluating this pressure  $p_{\text{rad},w}$  at the bubble wall, we have

$$G \equiv R(H + \dot{R}^2/2), \quad (9)$$

$$p_{\text{rad},w} = \frac{1}{b\Gamma} \left[ \frac{2}{\Gamma + 1} + \frac{\Gamma - 1}{\Gamma + 1} \left( 1 + \frac{\Gamma + 1}{Rc_0^2} G \right)^{1/2} \right]^{2\Gamma/(\Gamma-1)} - B. \quad (10)$$

This particular formulation for radiated pressure was described by Akulichev.<sup>24</sup>

To complement the preceding model for the radial dynamics in the liquid and close the formulation of the problem, it is necessary to determine the pressure inside the bubble. To this end,  $p_i$  can be estimated by enforcing conservation of mass, momentum, and energy in the gas phase. As argued by Prosperetti *et al.*,<sup>34</sup> the momentum equation can be used to justify an assumption of uniform pressure within the bubble. In addition, they demonstrated that continuity and energy relations can be used to derive both an ODE for the evolution of pressure inside the bubble and a partial differential equation (PDE) for temperatures in the gas phase. Ultimately, Prosperetti *et al.* concluded that enforcing an energy balance on the bubble contents is superior to assuming a polytropic relation for calculating gas pressures in bubbles undergoing nonlinear oscillations.

In the cited work by Prosperetti *et al.*, no mass transport was allowed at the liquid-gas interface and the gas velocity at the interface was simply the bubble-wall velocity  $\dot{R}$ . However, if mass transport is not neglected and density in the gas phase is assumed spatially uniform, the radial gas velocity at the bubble wall is defined by the continuity equation:

$$u|_{r=R} = \dot{R} - \frac{R}{3} \frac{\dot{n}}{n}. \quad (11)$$

Here,  $n$  denotes the total number of moles of gas inside the bubble and the overdots again indicate time derivatives. Continuing the assumption of spatial uniformity inside the bubble, conservation of energy can then be expressed as

$$\dot{p}_i = \gamma p_i \left( \frac{\dot{n}}{n} - \frac{3\dot{R}}{R} \right) + (\gamma - 1) \frac{3k_g}{R} \frac{\partial \theta}{\partial r} \Big|_{r=R}, \quad (12)$$

where  $\gamma = c_p/c_v$  is the ratio of specific heats,  $k_g$  is the thermal conductivity of the gas phase, and  $\theta$  is the average temperature inside the bubble. This equation is identical to that used by Szeri<sup>12</sup> and is equivalent to that used by Toegel *et al.*<sup>35</sup> Again, note that Eq. (12) relies upon assumptions of ideal-gas behavior and spatial uniformity of thermodynamic variables. While the preceding equations in this section complete a formulation for the radial dynamics, implementation of Eq. (12) requires estimates of heat and mass transport across the bubble wall.

## B. Mass transport

For gas-vapor bubbles, mass transport must account for both vapor and non-condensable gases. Henceforth, the term “gas” will be used as a shorthand for non-condensable gases in the context of specific bubble contents. Accordingly, the total molar content of the bubble is given by  $n = n_g + n_v$ , where the “g” and “v” subscripts respectively denote gas and vapor. Inherent in this formulation is the assumption that any mixture of non-condensable gases can be treated effectively as a single gas with suitable physical properties. To determine the overall mass transport, rates of change of  $n_g$  and  $n_v$  are calculated separately. A schematic to represent the modeling of mass diffusion is provided in Fig. 1(a). In this schematic, note that the thick line represents the bubble wall and that the curvature implies a gaseous interior on the left-hand

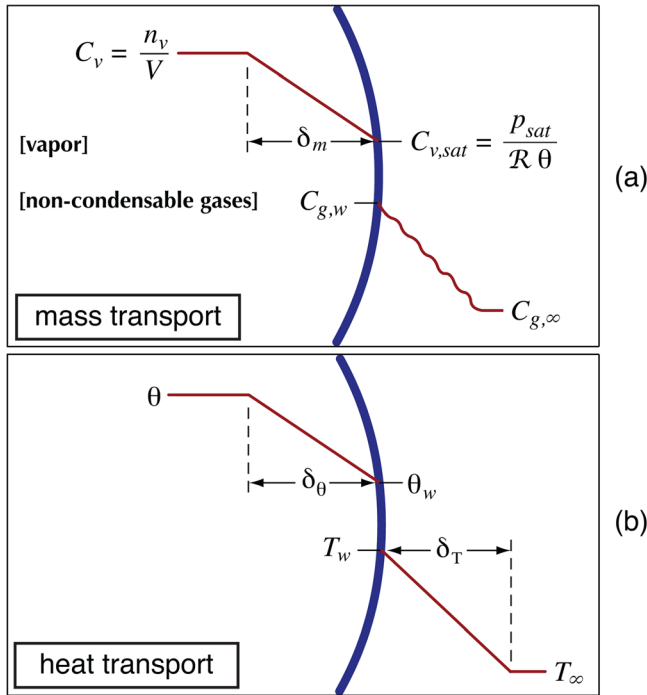


FIG. 1. (Color online) Schematic depiction of assumed boundary layers used in the model. In each diagram, the thick line represents the liquid-gas interface, whose curvature implies gas on the left and liquid on the right. (a) For mass transport,  $C$  denotes mass concentration, accompanying subscripts indicate the relevant substance and/or location, and  $\delta_m$  denotes the diffusive boundary-layer thickness inside the bubble. The wavy line in the liquid implies that no explicit boundary-layer thickness is assumed by the Eller-Flynn convolution for mass diffusion. (b) For heat transport,  $\theta$  and  $T$  denote temperatures in the gas and liquid, respectively. Thermal boundary-layer thicknesses are defined as  $\delta_\theta$  and  $\delta_T$ , where the explicit thickness  $\delta_T$  is assumed only in the SCL model.

side. Given a two-part mixture of gas and vapor, the molar concentration of vapor in the boundary layer is assumed to vary linearly between the average interior concentration  $C_v$  and a saturation concentration  $C_{v,sat}$  at the bubble wall. These concentrations at any given time may be calculated in terms of state variables for moles of vapor inside the bubble  $n_v$ , bubble volume  $V$ , the saturation vapor pressure of the liquid at the interface  $p_{sat}$ , the average temperature of the gas phase  $\theta$ , and the universal gas constant  $\mathcal{R}$ . The thickness of the boundary layer for mass diffusion inside the bubble is defined as  $\delta_m$  and is estimated in terms of the time scale for bubble motion and the diffusivity between two ideal gases. In the liquid, no explicit boundary layer for the diffusion of dissolved gases is assumed (as implied by the wavy line). The convective diffusion problem is instead solved approximately using boundary conditions representing the constant gas concentration far from the bubble  $C_{g,\infty}$  and the gas concentration at the bubble wall  $C_{g,w}$  as determined by Henry’s law and the instantaneous partial pressure of non-condensable gases inside the bubble.

### 1. Non-condensable gases

A classical solution for diffusion of dissolved gases in the liquid surrounding a spherical bubble was proposed by Eller and Flynn.<sup>22</sup> In this approach, Henry’s law provides an instantaneous boundary condition at the bubble wall, thereby coupling the thermodynamic state of non-condensable gases inside the bubble to the diffusion of these same gases in the surrounding liquid. Noting that the Eller-Flynn solution is uniformly valid in time only under equilibrium conditions at which there is no net mass flux to or from the bubble (i.e., the “high-frequency” solution), Fyrrilas and Szeri<sup>36</sup> developed a new solution that accounts for non-equilibrium conditions in which a diffusive boundary layer develops. However, their approach requires a splitting of the problem into smooth and oscillatory components and involves averaging over an oscillatory period of bubble motion. For simplicity, we follow Church<sup>10</sup> and adopt the zeroth-order Eller-Flynn solution to capture the basic features of diffusion for transient bubble motion. This approach has been successfully utilized to study mass diffusion in lithotripsy bubbles.<sup>10,11</sup> As noted previously, implementation of the Eller-Flynn solution does not require explicit estimation of the boundary-layer thickness.

To state the zeroth-order Eller-Flynn solution, we first define a time scale for diffusion in terms of the actual time  $t$  and the bubble radius  $R$  as

$$\tau = \int_0^t R^4 dt'. \quad (13)$$

Next, we define the concentration difference that drives diffusion as  $\mathcal{F} \equiv C_{g,w} - C_{g,\infty}$ , where  $C_{g,w}$  is defined by Henry’s law and  $C_{g,\infty}$  can now be interpreted as the initial concentration everywhere in the liquid. Identifying  $\mathcal{H}$  as the inverse of Henry’s constant, the saturation concentration at the bubble wall can then be instantaneously calculated as  $C_{g,w} = \mathcal{H}p_i (n_g/n)$ . Now, taking  $n_{g0}$  to represent  $n_g$  at time

$t = 0$ , we estimate diffusive transport effects through the following convolution calculation:

$$n_g = n_{g0} - 4\sqrt{\pi\mathcal{D}} \int_0^\tau \frac{\mathcal{F}(\tau')}{\sqrt{\tau - \tau'}} d\tau'. \quad (14)$$

Note that  $\mathcal{D}$  in this equation is the diffusion constant of the non-condensable gas in the liquid. From this solution, the current amount of non-condensable gas inside the bubble may be calculated at a given time for a given bubble radius. However, at any specified time, the calculated value for  $n_g$  relies upon an estimated value for  $p_i$ , which is in turn a function of  $n_g$ . To address this circular dependence, Church<sup>10</sup> suggested that sequentially updating  $n_g$  and  $p_i$  three times provides a reasonably accurate convergence for lithotripsy bubbles. For computational convenience, an adaptation of this approach was used here and is described further in the ensuing section on numerical implementation.

## 2. Vapor

The model for evaporation and condensation at the bubble wall is based on the kinetic theory of ideal gases and has been used in various other bubble models. Neglecting effects associated with the curvature of the liquid-gas interface and any bulk motion of vapor relative to the interface, the net flux of vapor into the bubble may be estimated by summing both evaporative and condensative fluxes as follows<sup>37</sup>:

$$\dot{n}_v = 4\pi R^2 \frac{\hat{\sigma}}{\sqrt{2\pi M R T_w}} (p_{\text{sat}} - f p_i). \quad (15)$$

Here,  $\dot{n}_v$  is again the time rate of change of the number of moles of vapor inside the bubble,  $T_w$  is the liquid temperature at the bubble wall,  $p_{\text{sat}}$  is the saturated vapor pressure evaluated at  $T_w$ ,  $\hat{\sigma}$  is an accommodation coefficient, and  $M$  is the vapor's molecular weight. In addition,  $f = n_v/n$  is the vapor fraction such that  $f p_i$  represents the partial pressure of vapor inside the bubble. Note that Eq. (15) assumes that the vapor temperature at the interface is effectively equal to the liquid temperature  $T_w$  for estimating the evaporative flux. Based on molecular dynamics simulations,<sup>17</sup> we select a value  $\hat{\sigma} = 0.4$  for the accommodation coefficient.

Strictly speaking, the above kinetic equation for phase change only applies for a pure vapor bubble below the critical temperature of the liquid. Above the critical temperature, no transport occurs since the phases are ill-defined. Following Akhatov *et al.*,<sup>38</sup>  $\dot{n}_v$  is identically set to zero when either the vapor temperature  $\theta$  or the liquid temperature  $T_w$  exceeds the critical temperature  $T_c$  of the liquid. In addition, if non-condensable gases are present, diffusion in the bubble interior among vapor and non-condensable gas molecules must also be considered. In particular, such diffusion is important when the time scale for diffusion is much slower than the time scale for bubble motion. Following other reduced-order models,<sup>12,35</sup> we associate evaporation with bubble growth and conditions in which the expanded volume allows the incoming vapor flux to occur without being limited by the presence of non-condensable gases inside the bubble. Con-

versely, we expect that condensation during a bubble's collapse leads to the evolution of a dense layer of non-condensable gas molecules near the bubble wall. Accordingly, the condensation rate is limited by the need for vapor molecules to diffuse past non-condensable gas molecules in order to reach the liquid-gas interface. This phenomenon has been described as "vapor trapping."<sup>17</sup>

Again following the aforementioned reduced-order models, we assume that gas-vapor diffusion can be approximated with a linear concentration gradient near the boundary, as depicted in Fig. 1(a). Then, the diffusive flux can be estimated with the Fickian relation

$$(\dot{n}_v)_{\text{max,cond}} = 4\pi R^2 \mathcal{D}_{12} \frac{C_v - C_{v,\text{sat}}}{\delta_m}, \quad (16)$$

where  $\mathcal{D}_{12}$  is the diffusion coefficient between vapor and non-condensable gas molecules,  $C_v = n_v/V$  is the molar concentration of vapor inside the bubble,  $C_{v,\text{sat}}$  is the equilibrium concentration at the surface temperature  $T_w$ , and  $\delta_m$  is the boundary layer thickness for mass diffusion. Considering the time scale for bubble motion as the volumetric ratio  $V/|\dot{V}|$  and introducing  $A_m$  as an arbitrary scale factor, the thickness  $\delta_m$  can be estimated as a characteristic diffusive penetration distance:

$$\delta_m = A_m \sqrt{\mathcal{D}_{12} \left( \frac{R}{3|\dot{R}|} \right)}. \quad (17)$$

The diffusive flux implied by Eqs. (16) and (17) sets a maximum condensation rate. When the kinetic Eq. (15) implies condensation in excess of the diffusive flux, the diffusive flux defines the rate of condensation.

To complete the model description with regard to vapor trapping behavior, several additional details need to be specified. First, note that  $\delta_m$  is constrained to remain less than or equal to the bubble radius. In addition, the singularity at  $|\dot{R}| \approx 0$  is handled by setting a minimum value for  $|\dot{R}|$ . Model results were found to converge when minimum values on the order of 1 m/s or smaller were used. Accordingly, a minimum value of  $10^{-3}$  m/s was adopted as a relatively small radial velocity that does not introduce numerical artifacts. Last, we must specify the arbitrary scaling factor  $A_m$  and the conditions that distinguish behaviors of a "pure" vapor bubble from those of a gas-vapor bubble that can exhibit vapor-trapping behavior. As discussed further in Sec. IV A, experimental data for the collapses of millimeter-sized lithotripsy bubbles<sup>19</sup> suggest that vapor trapping can be modeled via Eq. (16) when the vapor fraction  $f$  is less than some critical value  $f_m$ . Using model parameters  $f_m = 0.998$  and  $A_m = 0.8$  produces model predictions that agree well with these experimental data.

## C. Heat transport

In Fig. 1(b), boundary-layer assumptions for heat transport are shown. Considering the total energy of the bubble's contents and an ideal-gas equation of state, the homogeneous interior temperature  $\theta$  is first calculated. Because the gas

temperature at the bubble wall  $\theta_w$  depends on both the interior gas temperature and the liquid temperature at the interface  $T_w$ , a thermal boundary layer with thickness  $\delta_\theta$  exists. As before, the boundary layer thickness is estimated from the time scale of bubble motion and the thermal diffusivity of the gas phase. In the presence of thermal conduction at the liquid-gas interface, gas dynamics simulations suggest that a finite temperature difference  $T_w - \theta_w$  can be estimated between phases.<sup>39,40</sup> As the final piece of the heat transport model, the liquid temperature  $T_w$  is determined from the heat flux at the bubble wall and the temperature far from the bubble  $T_\infty$  using either the approximate solution of the PZ model or the Fickian approach of the SCL model. Although not depicted in the figure, no explicit boundary layer thickness is assumed in the PZ model. In the SCL model, a linear boundary layer between the temperatures  $T_w$  and  $T_\infty$  is assumed and the boundary-layer thickness is defined as  $\delta_T$ . Because heat transport in the gas and liquid phases are obviously coupled,  $\theta_w$ ,  $T_w$ , and the implied temperature gradients must be solved conjunctively. Moreover, it is noteworthy that phase change at the bubble wall affects both heat- and mass-transport calculations. Hence, both heat and mass transport must be solved simultaneously.

Calculating heat transport behavior requires the balancing of three thermal processes at the bubble wall: thermal conduction in the gas, thermal conduction in the liquid, and the heat of vaporization associated with phase change. Given Eq. (15), heat and mass transport are directly coupled through  $T_w$  and  $\dot{n}_v$ . Both the PZ and SCL models use the same approach for estimating the temperature gradient in the gas phase, the total energy balance at the liquid-gas interface, and the temperature jump between liquid and gas phases. The temperature gradient in the gas is required by Eq. (12) for the radial dynamics and is estimated from the following relations:

$$\left. \frac{\partial \theta}{\partial r} \right|_{r=R} = \frac{\theta_w - \theta}{\delta_\theta} \quad (18)$$

$$\delta_\theta = A_\theta \left( \frac{k_g}{\rho_m c_p} \frac{R}{\sqrt{p_i/\rho_0}} \right)^{1/2}. \quad (19)$$

Here  $A_\theta$  is an arbitrary constant,  $\rho_m$  is the density of gases inside the bubble,  $c_p$  is the constant-pressure specific heat of the gas-vapor mixture, and  $\rho_0$  is again the ambient liquid density. Note that  $R(p_i/\rho_0)^{-1/2}$  is used as a time scale for bubble motion in this definition of  $\delta_\theta$ , which is required to remain less than or equal to the bubble radius. Unlike that used above for  $\delta_m$ , this time scale possesses no singularities and is beneficial for estimating thermal behavior during collapse. Incidentally, this time scale is not well suited to estimating the aforementioned mass diffusion. Upon comparison with a sample calculation presented by Preston,<sup>18</sup> the value  $A_\theta = 0.5$  was found to provide a good approximation to the thermal boundary-layer thickness for a bubble undergoing an inertial collapse.<sup>41</sup> Hence, this value is adopted here.

Both the SCL and PZ models also employ the same relations for enforcing an energy balance at the bubble wall and

for calculating the temperature difference  $T_w - \theta_w$ . Respectively, these relations can be expressed as

$$4\pi R^2 k_g \left. \frac{\partial \theta}{\partial r} \right|_{r=R} - 4\pi R^2 k_\ell \left. \frac{\partial T}{\partial r} \right|_{r=R} + \dot{n}_v \mathcal{L} + \dot{n}_{c_v} (\theta_w - T_w) = 0 \quad (20)$$

$$T_w - \theta_w = \zeta \left( \frac{V}{\sqrt{2\pi n} \mathcal{N}_A \Omega^2} \right) \left. \frac{\partial \theta}{\partial r} \right|_{r=R}. \quad (21)$$

In the first equation,  $k_g$  and  $k_\ell$  are the thermal conductivities in the gas and liquid,  $\mathcal{L}$  is the heat of vaporization, and  $c_v$  is the constant-volume heat capacity of the gas-vapor mixture. In the second,  $\zeta$  is the temperature-jump coefficient determined from kinetic gas models,  $\mathcal{N}_A$  is Avogadro's number, and  $\Omega$  is the hard-sphere molecular diameter as calculated from Lennard-Jones potentials. The parenthesized quantity in the second equation represents the mean-free path of gas molecules inside the bubble.<sup>40,42</sup> Although it is unclear that a nonzero temperature difference  $T_w - \theta_w$  need be considered,<sup>41</sup> this modeling component is included for generality and consistency with prior work.<sup>43,44</sup> Although it is difficult to extrapolate the results from kinetic gas simulations to the conditions present in a collapsing bubble, values of  $\zeta$  calculated by Sharipov and Kalempa<sup>40</sup> suggest that likely values range from about 2 to 2.5. We select a value  $\zeta = 2$  here as a round number—results suggest that the model is not sensitive to this parameter. In addition to Eqs. (18)–(21), either the PZ or the SCL model as described below is used to calculate the liquid temperature  $T_w$ .

### 1. Plesset-Zwick (PZ) model

The problem of thermal conduction in the liquid is completely analogous to the Eller-Flynn solution for the diffusion of dissolved gases as described in Sec. II B 1. Using the same time scale  $\tau$  from Eq. (13), the convolution integral for the liquid temperature can be written as

$$T_w = T_\infty - \sqrt{\frac{k_\ell}{\rho_0 c_{p\ell}}} \int_0^\tau \frac{\mathcal{F}_{PZ}(\tau')}{\sqrt{\tau - \tau'}} d\tau' \quad (22)$$

$$\mathcal{F}_{PZ} = \frac{1}{R^2} \left. \frac{\partial T}{\partial r} \right|_{r=R} \quad (23)$$

where  $c_{p\ell}$  is the heat capacity of the liquid. To implement the PZ model, the temperature gradient in Eq. (23) is found algebraically from Eq. (20) as a function of  $\theta$ ,  $\theta_w$ ,  $T_w$ ,  $\dot{n}_v$ , and  $\dot{n}$ . Further details of the model implementation are deferred to Sec. III

### 2. Scaling (SCL) model

Unlike the PZ model, the SCL model utilizes an explicit assumption of a linear temperature gradient in the liquid, as depicted in Fig. 1(b). Accordingly, this gradient is approximated as

$$\left. \frac{\partial T}{\partial r} \right|_{r=R} = \frac{T_\infty - T_w}{\delta_T}. \quad (24)$$

To estimate the boundary-layer thickness  $\delta_T$ , one approach is to consider thermal conduction and to adopt the same time scale for bubble motion that was used for  $\delta_\theta$ . Omitting any arbitrary scaling constant, this approach yields

$$\delta_{T1} = \left( \frac{k_\ell}{\rho_0 c_{p\ell}} \frac{R}{\sqrt{p_i/\rho_0}} \right)^{1/2}. \quad (25)$$

However, it is important to recognize that phase change at the interface introduces another relevant time scale. Considering a thin shell of liquid whose thickness is  $\delta_{T2}$ , we approximate the mass of liquid in this shell as  $\rho_0 4\pi R^2 \delta_{T2}$ . Assuming a uniform temperature within the shell and considering heat transfer only due to phase-change processes, a new time scale can be estimated as a function of the boundary-layer thickness  $\delta_{T2}$  and the rate of evaporation or condensation. Introducing this time scale into the same definition of thermal penetration distance used in Eq. (25), we can solve for the thickness:

$$\delta_{T2} = \frac{4\pi R^2 k_\ell}{\mathcal{L} |\dot{n}_v|}. \quad (26)$$

This boundary-layer approximation effectively assumes that thermal conduction on the inner and outer surfaces of the liquid shell offset one another, while convection is negligible. Such conditions are most consistent with slow-moving phases of bubble motion.

Although various schemes for defining an effective boundary-layer thickness can be conceived, we define it simply as the minimum of  $\delta_{T1}$  and  $\delta_{T2}$ . Introducing the arbitrary scaling constant  $A_T$ , we have

$$\delta_T = A_T \times \min\{\delta_{T1}, \delta_{T2}\}. \quad (27)$$

For an inertially collapsing bubble,  $\delta_{T2}$  typically remains less than  $\delta_{T1}$  until the late stages of collapse when the critical temperature of the liquid is exceeded and phase change ceases. As discussed in Ref. 41 and demonstrated in Fig. 7(c), the scaling implied by  $A_T = 1.3$  yields roughly the same estimate of  $T_w$  as the PZ model.

### III. MODEL IMPLEMENTATION

The model equations described in the preceding section were numerically solved under various conditions to elucidate the role of vapor. The numerical implementation comprises two basic steps. First, the model equations are formulated in state-space form as  $\dot{y} = f(y, t)$ , where  $y$  is the state vector,  $t$  is time, and the overdot denotes a time derivative. Second, the state equations are integrated in Fortran95<sup>45</sup> using a fifth-order Runge-Kutta routine with explicit time marching and variable time steps. The Runge-Kutta routine includes error estimates by also evaluating an embedded fourth-order solution.<sup>46</sup> The variable step size during integration is chosen so that the relative error for each state variable remains less than a prescribed nondimensional tolerance. Further details of the implementation are described below; additional discussion of the numerical solution is available in Ref. 41.

### A. Function evaluations

Because each successful integration step requires an evaluation of the time derivative of state variables  $\dot{y}$ , it is insightful to consider what each of these function evaluations entails. To this end, we first note that the state variables are defined as bubble radius and velocity ( $R, \dot{R}$ ), pressure  $p_i$ , moles of non-condensable gas  $n_g$ , and moles of water vapor  $n_v$ . While these variables technically define the state of the bubble for integration, they do not account for any changes in the gas and liquid temperatures at the bubble wall. Indeed,  $T_w, \theta_w, \dot{n}_v$ , and  $\dot{p}_i$  are intimately coupled. Hence, performing a function evaluation requires a substep in which  $T_w$  and  $\theta_w$  are determined self-consistently with derivatives of the state variables. In addition, each function evaluation involves an interdependence between  $\dot{p}_i$  and the rate of change of  $n_g$  as implied by Eq. (14). This interdependence can also be addressed with substep calculations.

Because the temperatures  $T_w$  and  $\theta_w$  affect heat and mass transport, substep calculations are used to “settle” their values in conjunction with the estimated derivative  $\dot{n}_v$ . To this end, we adopt an iterative approach similar to that used by Church for a gas bubble.<sup>10</sup> Each iteration comprises the following steps: (1) evaluation of  $\dot{n}_v$  based on present values of the state variables and the average temperature  $\theta$  implied by the ideal gas equation, (2) calculation of  $T_w$  and  $\theta_w$  using either the PZ or the SCL model, and (3) evaluation of the change in  $T_w$  relative to the value computed after the last completed time step. These steps are repeated in successive iterations until either the relative change in  $T_w$  is less than 1% or more than 10 iterations have been executed. After exiting the iteration loop, the values of  $T_w, \theta_w$ , and  $\dot{n}_v$  are considered “settled” for a given function evaluation such that  $\dot{p}_i$  and other state derivatives can be calculated. With this approach, a few iterations are often sufficient to achieve convergence of the thermal variables. However, during very violent collapses, convergence to within 1% relative error may not be reached even after tens or hundreds of iterations. Accordingly, the maximum number of iterations was selected as 10 for computational efficiency.

Having defined the thermal substep, we now describe the estimation of  $\dot{n}_g$ . Church used substep calculations whereby the gas partial pressure  $(n_g/n)p_i$  and the updated gas content  $n_g$  were iteratively calculated using the ideal gas equation and Eq. (14). He found that reasonable convergence was achieved in three iterations.<sup>10</sup> Here, an alternate approach is implemented based upon the recognition that the diffusive time scale is considerably longer than typical integration time steps. To take advantage of the relative slowness of diffusion, the time derivative during the  $k$ th time step is estimated from the previous time step as

$$\dot{n}_g = \frac{n_g^{(k)} - n_g^{(k-1)}}{t^{(k)} - t^{(k-1)}}, \quad (28)$$

where the parenthesized superscripts denote the relevant integration steps. Using this estimate of the derivative,  $n_g^{(k+1)}$  is initially estimated from the Runge-Kutta integration and is then updated by performing the convolution of Eq. (14) with

the current state variables  $y^{(k+1)}$ . This approach was found to yield results very similar to Church's while being more computationally efficient.

## B. Convergence behavior

For a numerically convergent model, the smaller time steps required by smaller error tolerances produce more accurate results. However, as discussed above, the present model includes substep operations for thermal variables as well as for mass diffusion of dissolved gases. In addition, smaller time steps become increasingly troublesome for evaluating the convolution integrals used to determine either  $T_w$  (in the PZ model) or  $n_g$ . Overall, the SCL and PZ models were typically found to converge for error tolerances on the order of  $10^{-6}$  or smaller when considering a single Rayleigh collapse.<sup>41</sup> However, very small time steps associated with smaller tolerances for the PZ model tend to produce noisy results from the convolution calculation for  $T_w$ , possibly leading to numerical instabilities during violent collapses. As a result, for any attempted time step in which the PZ model yields an unrealistic estimate of  $T_w$  (e.g., below the melting point of the liquid or “NaN”), the SCL model is utilized to provide the estimate. This strategy enables the PZ model to be successfully extended to collapses that are otherwise numerically intractable.

Aside from numerical convergence characteristics *per se*, another observation of model stability and performance was noted. Numerical performance is much better when heat conduction in both the liquid and the gas are considered. More specifically, if  $T_w$  is assumed to remain constant, the model requires extremely small step sizes and often does not effectively integrate through a collapse. This behavior can be explained by recognizing that a fixed liquid temperature leads to an overprediction of the temperature gradient in the gas during collapse. Through Eq. (12), the overestimated temperature gradient enhances the coupling of radial dynamics with heat transport. Because the thermal variables are addressed in a substep rather than by direct integration as state variables, very small steps are required to “settle” the thermal variables. We conclude that even though the iteration limit of 10 may be exceeded during collapses, the allowance of liquid heating nonetheless facilitates a more consistent estimation of temperature gradients and improves numerical performance.

## C. Fluid properties

A final aspect of the model implementation involves the fluid properties used for liquid and gas phases. The model was implemented to represent an air bubble in water. Table I displays the relevant properties, functional dependencies, and references from which associated formulations were adopted. Many of the same or similar formulations have been used in previous bubble models.<sup>35,43,47</sup> In the table, note that the properties are divided into three groups: in the top group, properties are initialized and not updated during integration; in the middle group, properties are updated after each integration time step; in the bottom group, properties are updated during each time step as an inherent part of the integration. To evaluate any fluid property under conditions

TABLE I. Fluid properties for water and air.

Property	Dependency	Reference #
liquid saturation density	$\rho_0(T_\infty)$	62
liquid sound speed	$c_0(T_\infty)$	63, 64
liquid heat capacity	$c_{pl}(T_\infty)$	65
liquid-gas diffusivity	$\mathcal{D}(T_\infty, p_0)$	66
liquid viscosity	$\mu(T_w, p_w)$	67
liquid-gas surface tension	$\sigma(T_w)$	68
gas-liquid solubility	$\mathcal{H}(T_w)$	69
liquid thermal conductivity	$k_l(T_w, p_w)$	67
gas thermal conductivity	$k_g(\theta, \rho_m, f)$	47, 70
saturation vapor pressure	$p_{sat}(T_w)$	62
latent heat of vaporization	$\mathcal{L}(T_w)$	71
gas heat capacity	$c_v(\theta, f)$	42
gas heat capacity	$c_p = c_v + \mathcal{R}$	ideal gas
two-gas diffusivity	$\mathcal{D}_{12}(\theta, \rho_m, f)$	42, 70

beyond the range specified for the referenced correlation, the closest conditions within the specified range were used.

The model is quantitatively sensitive to fluid properties and their implementation (see Sec. IV B 1. below). Moreover, for applications involving therapeutic ultrasound, the relevant physical properties of biological fluids remain difficult to define. However, simulating an air bubble in water provides insight into both the relative importance of specific properties and qualitative trends in the bubble dynamics for a given application. In addition, even though the model is not currently formulated to treat viscoelastic fluid properties, such an adaptation could be made.<sup>48</sup>

## IV. VALIDATION

To validate model performance, numerical results are presented in two subsections below. First, model predictions are compared with experimental data to identify suitable values for the parameters  $A_m$  and  $f_m$  that describe the diffusive behavior of vapor inside the bubble. Next, benchmark simulations are compared against the predictions of several models from the literature in order to quantify the relative performance of the present reduced-order model.

### A. Model tuning

From the model presented above, two parameters associated with vapor transport were not determined. These parameters are associated with diffusion among vapor and non-condensable gas molecules inside the bubble and thus affect how vapor is trapped when diffusion limits the condensation rate implied by gas kinetics. More specifically, the parameter  $A_m$  scales the thickness of the diffusive boundary layer, while  $f_m$  indicates the critical molar fraction of vapor inside the bubble below which vapor trapping is controlled by diffusion per Eq. (16). To complete the model description, it is necessary to identify values for these parameters. The approach taken here is to use experimental observations of individual bubble collapses to guide parameter identification.

To investigate vapor transport during a single inertial collapse, bubbles excited by lithotripter shock waves provide

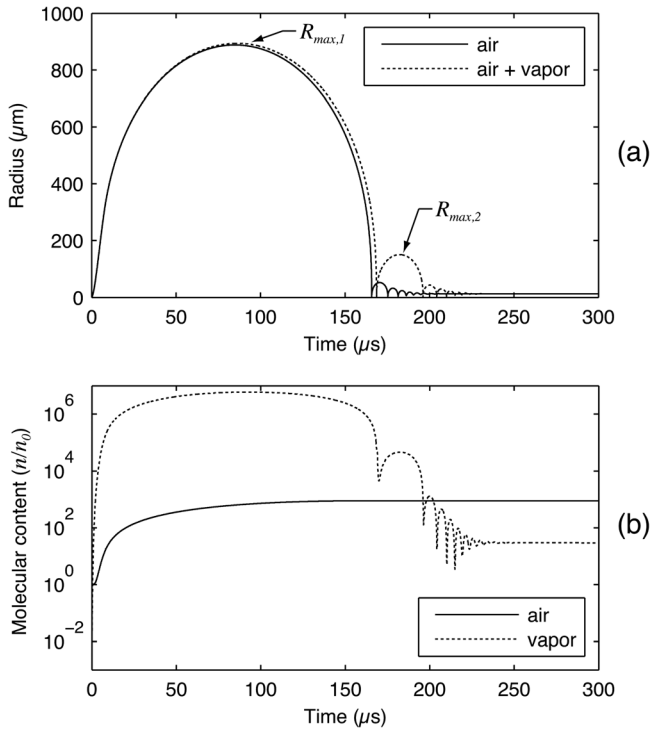


FIG. 2. Characteristic dynamics of a micron-sized bubble in water after excitation by a lithotripter shock wave. (a) Radius-time curves for an air bubble and an air-vapor bubble demonstrate that vapor affects the bubble rebound even in the absence of vapor trapping. (b) A plot showing the composition of the air-vapor bubble as a function of time.

a useful subject for study. As suggested by Church,<sup>10</sup> the negative tail of a lithotripter shock wave leads to prolonged bubble growth followed by an unforced Rayleigh collapse several hundred microseconds later. Also, as noted by Matula *et al.*,<sup>12</sup> the amount of vapor inside the bubble exceeds the amount of non-condensable gas throughout most of the bubble motion. These qualitative dynamics are illustrated in Fig. 2. In Fig. 2(a), the radial dynamics of an air bubble are shown for cases in which vapor is and is not excluded from the bubble. Figure 2(b) shows the relative evolution of air and vapor content for the latter case. Note that to generate this figure, the present model was used while vapor trapping per Eq. (16) was neglected. These calculations imply that lithotripsy bubbles consist mostly of vapor during collapse, even in the absence of vapor trapping. Moreover, as suggested by the rebounds after the main collapse at roughly 165  $\mu\text{s}$ , the presence of vapor significantly affects the energy lost during collapse. Since vapor transport is expected to be a function of both the temperature of the surrounding liquid and diffusive interactions with non-condensable gases inside the bubble, these transport processes can be explored by observing the rebounds of lithotripsy bubbles while ambient water conditions are varied across a range of temperatures and dissolved gas concentrations.

Such experiments with lithotripsy bubbles were conducted and are described in detail elsewhere.<sup>19</sup> These experiments comprised photographic observations of individual bubble collapses and rebounds in water, using a matrix of nine test conditions. Each condition for the water was characterized by one of three temperatures (20, 40, or 60 °C) and

one of three levels of dissolved atmospheric gases (measured as dissolved oxygen concentrations at 10%, 50%, or 85% of saturation). Because data collection at 60 °C, 85% dissolved oxygen was complicated by the sequence of water processing and the apparent spontaneous growth of supersaturated carbon dioxide bubbles, only data from the other eight conditions were considered in evaluating best-fit values for the model parameters  $A_m$  and  $f_m$ .

For each observed collapse and rebound, the dynamics were quantified by the fraction of energy retained by the bubble through the collapse. For the characteristic bubble motion illustrated by the dashed line in Fig. 2(a), the radial velocity is zero when the maximum radii  $R_{\text{max},1}$  and  $R_{\text{max},2}$  are reached. Moreover, because there is no external forcing after the initial few microseconds of the plot, the bubble's energy before and after collapse can be defined in terms of the energy required to expand the bubble's volume against the pressure difference between the bubble interior and the surrounding liquid. Assuming a quasistatic expansion, the liquid pressure  $p_0$  and the vapor pressure inside the bubble  $p_{\text{sat}}$  remain constant. Accordingly, the ratio  $(R_{\text{max},2}/R_{\text{max},1})^3$  represents the fraction of energy retained by the bubble after collapse and is used here to characterize the bubble dynamics. Essentially the same normalization approach was previously adopted for evaluation of laser-induced cavitation bubbles.<sup>49</sup>

In addition to normalization, each observed collapse was also categorized based on the presence or absence of a visible re-entrant jet. The presence of a jet was used to identify asymmetries, which can reduce the energy lost during violent collapses that are associated predominantly with acoustic radiation losses.<sup>49</sup> In the data reported in Ref. 19 asymmetries lead to definitively more energetic rebounds for the most violent collapses (i.e., those occurring at 20 °C as well as those at 40 °C, 10% dissolved oxygen). However, this trend essentially disappears for the other test conditions. Hence, in order to compare observations with model predictions that implicitly assume sphericity, calculated statistics exclude asymmetric collapses for the conditions explicitly cited above and include all collapses for the remaining conditions that are insensitive to asymmetries. As such, experimental data are plotted against model predictions in Figs. 3 and 4. In both figures, the mean for each test condition is plotted as a circle, with vertical bars extending  $\pm 1$  standard deviation.

For determining the model parameters  $A_m$  and  $f_m$ , it is insightful to consider separately the model sensitivity to both dissolved gas content and temperature. In Fig. 3, these sensitivities are explored for three different combinations of parameters: (1)  $f_m = 0.997$ ,  $A_m = 1.69$ ; (2)  $f_m = 0.998$ ,  $A_m = 0.80$ ; and (3)  $f_m = 0.999$ ,  $A_m = 0.524$ . The sensitivity to dissolved gas concentration at 20 °C is shown in Fig. 3(a), while Fig. 3(b) depicts the sensitivity to temperature at a dissolved gas concentration of 50%. For these plots, the PZ model was used for all simulations. Also, note that for each of the labeled molar fractions  $f_m$  in the figure, the aforementioned boundary-layer scaling for diffusion  $A_m$  is automatically implied.

As is evident in Fig. 3(a), the corresponding values for  $A_m$  were chosen so that bubbles would be predicted to retain

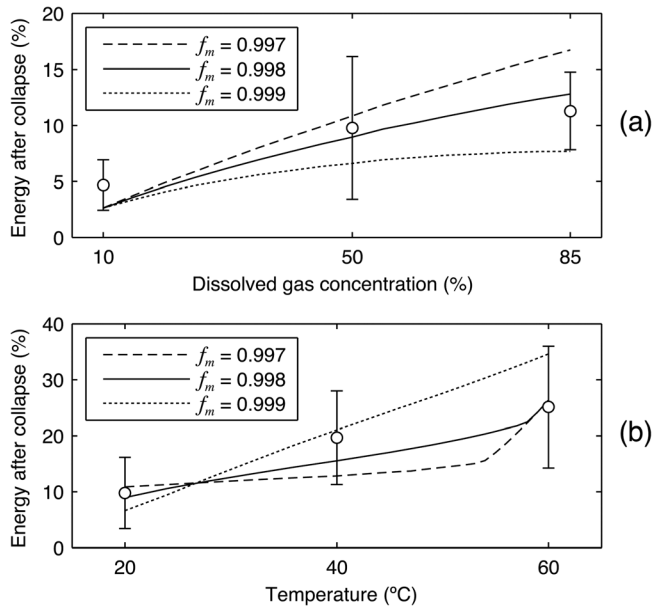


FIG. 3. Illustration of model sensitivities to the tuning parameters that represent the boundary-layer scaling for mass diffusion inside the bubble  $A_m$  and the critical molar fraction of vapor below which vapor trapping occurs  $f_m$ . The energy retained after the collapse of a lithotripsy bubble is plotted for various combinations of tuning parameters and water conditions. For each labeled value of  $f_m$ , a value of  $A_m$  is implied in order to predict bubble rebounds that retain 2.6% of their initial energy under water conditions at 20 °C and 10% dissolved oxygen. The corresponding model conditions are  $f_m = 0.997$  and  $A_m = 1.69$ ;  $f_m = 0.998$  and  $A_m = 0.8$ ;  $f_m = 0.999$  and  $A_m = 0.524$ . Open circles and associated vertical bars represent the mean  $\pm 1$  standard deviation of experimental observations at each water condition.<sup>19</sup> (a) Model sensitivity is plotted relative to reported observations at 20 °C and three separate dissolved oxygen concentrations. Experimental data at 10%, 50%, and 85% concentrations include 12, 13, and 6 independent bubble collapses, respectively. (b) Model sensitivity is plotted relative to data at 50% dissolved oxygen and three temperatures. Experimental data at 20, 40, and 60 °C include 13, 20, and 43 independent collapses, respectively.

about 2.6% of their energy after a collapse under conditions at 20 °C and 10% dissolved gas concentration. The model is specifically forced to fit this data point because collapses under such conditions have been independently explored. Akhatov *et al.*<sup>38</sup> examined the spherical collapses of millimeter-sized, laser-induced bubbles and found that bubbles retained about 2.4% of their energy. They reported data collection in a cuvette of distilled water at 23 °C. Although they did not specify any measured concentration of dissolved gases, we interpret “distilled” to imply a relative absence of dissolved gases. Hence, their result of 2.4% retained energy is comparable to observations from Fig. 3(a) at 10% dissolved oxygen. Because collapses under this condition were particularly sensitive to asymmetries and because the lack of a visible re-entrant jet did not preclude the presence of an asymmetry, it is reasonable to consider the lower observed values as indicative of truly spherical collapses. Indeed, the smallest several rebounds effectively match the rebound energy of 2.4% moreover, no asymmetries were apparent in any of the corresponding collapses.<sup>19</sup> Taking other observations into account, a slightly higher level of 2.6% was used for parameter determinations.

With the approach discussed above to select  $A_m$  for a given  $f_m$ , the values of  $f_m$  were in turn chosen to fit overall observations of sensitivity to dissolved gas concentration

and temperature. In both Fig. 3(a) and 3(b), it is evident that using  $f_m = 0.998$  most accurately fits the central tendencies of experimental observations. It is instructive to note that the model with  $f_m = 0.999$  is not sensitive enough to dissolved gases, but too sensitive to temperature. The opposite behavior is apparent for  $f_m = 0.997$ . Hence, because  $A_m$  is positively correlated with retained energy for all test conditions, adjustment of the  $A_m$  values (by relaxation of the requirement to fit 2.6% rebounds) would still not improve the overall fits for  $f_m = 0.997$  or 0.999. A final observation from this figure is that the simulations with  $f_m = 0.997$  and 0.998 converge as temperatures approach 60 °C. This convergence indicates an insensitivity to  $A_m$  and  $f_m$  whereby vapor trapping effects are not important. As such, at 60 °C and 50% dissolved oxygen, the bubble’s collapse is not dependent upon the amount of non-condensable gas inside the bubble; rather, the collapse is thermally controlled by the liquid temperature at the bubble wall.

For a comprehensive comparison of experimental observations with simulations based on the present reduced-order modeling approach, Fig. 4 includes all test conditions as well as simulations that use variations of the PZ and SCL models. All model calculations used in this figure utilize the parameters  $f_m = 0.998$ ,  $A_m = 0.8$ . First, we note that the PZ model simulates experimental observations well for all conditions except 60 °C, 85% dissolved oxygen. As mentioned above, data collected under these conditions were not considered reliable and are only shown here for completeness. Although the SCL model matches observations fairly well at 20 °C and 40 °C, it does not capture the behavior at 60 °C. Observations suggest that the dynamics are very similar at 60 °C and either 10% or 50% dissolved oxygen. However, the SCL model predicts a sizable difference between these

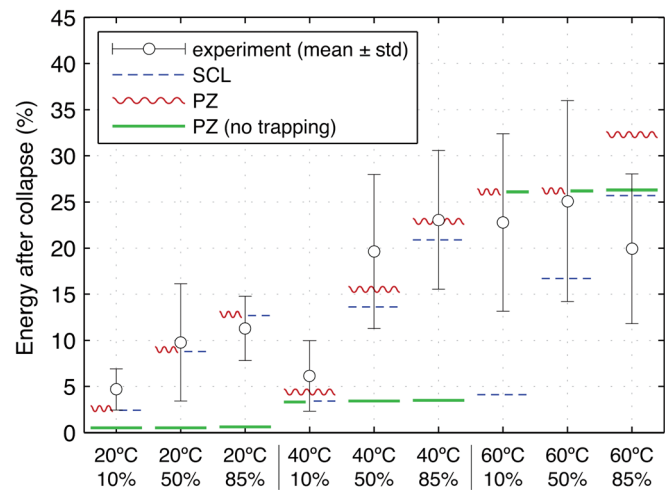


FIG. 4. (Color online) Comparison of various model predictions with experimental observations with regard to the energy retained after the collapses of lithotripsy bubbles. Two tuning parameters ( $f_m = 0.998$  and  $A_m = 0.8$ ) are used to fit eight separate groups of observations. Included here for completeness, the ninth experimental group at 60 °C and 85% dissolved oxygen was deemed unreliable given the presence of supersaturated carbon dioxide bubbles under the test conditions. Open circles and associated vertical bars represent the mean  $\pm 1$  standard deviation of experimental observations at each water condition.<sup>19</sup> Considering  $x$  axis conditions from left to right in the plot, experimental data represent 12, 13, 6, 5, 20, 23, 46, 43, and 22 independent bubble collapses, respectively.

conditions and underpredicts the amount of retained energy in both cases. In addition, calculations based on the PZ model in the absence of vapor trapping are plotted. By using the PZ model to estimate liquid temperatures while ignoring vapor trapping as described by the maximum condensation rate from Eq. (16), these calculations reflect thermal effects only. As demonstrated in Fig. 4, such a model complements the SCL model by matching the observations at 60 °C, but not at lower temperatures.

To interpret the performance of model calculations in Fig. 4, it is helpful to consider two independent mechanisms through which vapor can affect the dynamics of an inertial collapse. The first depends upon the diffusively controlled amount of vapor trapped in the bubble during collapse. In turn, the extent of vapor affects the evolution of pressure due to compression, whereby additional vapor slows the collapse and reduces the loss of energy. Because diffusion among vapor and gas molecules controls the amount of trapped vapor, this mechanism is fundamentally diffusive. The second mechanism relates to thermal interactions of vapor with the surrounding liquid. As a vapor bubble collapses and the liquid at the bubble wall is heated by both thermal conduction from the compressed gas and the latent heat associated with condensation, any increase in liquid temperature will increase the saturation vapor pressure and thereby arrest the collapse. This phenomenon can be described as a thermally controlled collapse. Because the SCL model algebraically estimates liquid temperature at each instant, the bubble's history and the potential evolution of a thermal boundary layer in the liquid are neglected. Consequently, the thermal effects of vapor that appear to become significant at 60 °C are not captured by the SCL model. Conversely, the PZ model with no limiting of condensation rates fails to simulate the diffusive effects of vapor even as the convolution used to estimate liquid temperature predicts the observed thermal effects.

In summary, for the eight conditions with reliable data, collapse dynamics are controlled mainly by diffusively controlled vapor trapping at 20 °C and 40 °C, while thermal effects dominate at 60 °C. The PZ model accurately simulates experimental observations for all eight conditions even though only two independent fitting parameters were used to tune the model. This good fit with an overdetermined set of experimental data provides validation that the present reduced-order model includes the essential physics relevant to the inertial collapses of millimeter-sized gas-vapor bubbles.

## B. Benchmark simulations

Above, the present reduced-order models were tuned and tested for the collapses of lithotripsy bubbles. However, it remains helpful to benchmark the PZ and SCL models against published results in order to clarify model capabilities and limitations, particularly with regard to heat and mass transport. Gas diffusion during low-amplitude, periodic bubble oscillations is commonly analyzed using the solution developed by Eller and Flynn.<sup>22,50</sup> However, for the large acoustic pressures and nonlinear bubble oscillations characteristic of therapeutic ultrasound, it is necessary to capture transient behavior. As such, transient diffusion calculations

are of interest, as represented here by the convolution Eqs. (14) and (22). Because bubble dynamics in therapeutic ultrasound are also characterized by violent inertial collapses, published model predictions relevant to sonoluminescence and HIFU also provide useful data for comparison. These two types of model benchmarks are described in detail in the following subsections.

### 1. Sensitivity to fluid properties

In making benchmark comparisons and drawing distinctions among various models, it is useful to understand the impact of the fluid properties. Unless explicitly noted otherwise, the definitions of fluid properties cited in Table I were used in the subsequent calculations. To examine the model's sensitivity to these properties, we consider changes in the rebounds of bubbles from two types of violent collapses: unforced collapses of millimeter-sized lithotripsy bubbles (at 20 °C, 10% dissolved gases), and forced collapses of the sonoluminescence bubble modeled by Storey and Szeri.<sup>17</sup> In both cases, changes in a bubble's simulated rebound are compared in terms of energy, which can be estimated as a ratio of the cube of rebound radii predicted for different fluid properties.

From Table I, we note that the middle and bottom groups of properties are of primary interest because static values were easily altered to make benchmark comparisons. In the middle group, only the thermal conductivities vary enough during an inertial collapse to alter the bubble's rebound appreciably. If the thermal conductivity of the gas-vapor mixture  $k_g$  is evaluated only at the initial conditions, the test lithotripsy bubble retains about 10% more energy after collapse, while the sonoluminescence bubble retains about 24% more energy with a fixed conductivity value. Similar trends are produced by fixing the liquid thermal conductivity  $k_l$ , though the changes in rebound energies are less by about an order of magnitude since  $k_g$  varies much more than  $k_l$  during a collapse. Because thermal conductivities are generally enhanced at higher temperatures and pressures, adjusting the effective values after each time step increases the thermal damping associated with the collapse. Despite the utility of the cited formulations for dynamically estimating thermal conductivities, such estimates still underestimate the true values near the supercritical region. Given the rather complex physical phenomena that may occur during violent collapses, the present model seeks only to capture the larger features of the dynamics.

In the bottom group,  $p_{sat}$  and  $\mathcal{L}$  are well defined properties for water that can be represented by straightforward correlations. On the other hand, gas properties for diffusivity  $\mathcal{D}_{12}$  and heat capacity  $c_v$  are more difficult to estimate under the extreme conditions associated with an inertial collapse. Because the present model is inherently sensitive to  $\mathcal{D}_{12}$  through a scaled boundary layer thickness [see Eq. (16)], it is not particularly insightful to explore the sensitivity to  $\mathcal{D}_{12}$  explicitly. However, the specific heat  $c_v$  can be estimated with or without a dependence on the temperature  $\theta$ . If the temperature dependence for  $c_v$  described in Ref. 42 is omitted, more energy is retained through collapse. Whereas thermal conductivity affects the collapse dynamics through thermal damping, the specific heat primarily affects acoustic damping. During

an inertial collapse, energy that goes to internal degrees of freedom is energy that does not contribute to the pressure inside the bubble. Hence, accounting for the temperature dependence of  $c_v$  leads to a lesser buildup of the pressure  $p_i$  at any given bubble radius. Accordingly, the bubble collapses to a smaller volume, achieves higher ultimate pressures as energy is more concentrated, and loses more energy by acoustic radiation. For the test lithotripsy bubble, the temperature dependence of  $c_v$  is more significant than variations in thermal conductivities; omitting the temperature dependence leads to a rebound with nearly 30% more energy. In contrast, a fixed heat capacity  $c_v$  leads to a retention of only about 6% more energy for the cited sonoluminescence bubble, which is considerably less than the additional energy retained with a fixed thermal conductivity  $k_g$ .

## 2. Application of convolution solutions

Application of the Eller-Flynn zeroth-order convolution solution to transient bubble motions was described by Church<sup>10</sup> and later duplicated by Sapozhnikov *et al.*<sup>11</sup> In both of these prior efforts, the diffusion of non-condensable gases was simulated for lithotripsy bubbles. Sapozhnikov *et al.* compared their model predictions with experimental observations of bubble dissolution times after passage of a shock wave. Using static overpressure as an independent variable, their observed dissolution times agreed well with calculations of transient gas diffusion into single bubbles excited by a shock wave. The net diffusion into an excited bubble was calculated with the zeroth-order convolution, while subsequent dissolution of a quiescent bubble was simulated with the Epstein-Plesset model.<sup>51</sup> For comparison with this prior work, the SCL model was used while neglecting vapor transport in order to calculate transient diffusion into lithotripsy bubbles. Model predictions shown in Fig. 5 are virtually identical to those reported by Sapozhnikov *et al.* Small discrepancies are attributable to differences in the fluid properties and disappear if the properties are fixed at their initial values while the liquid-gas diffusivity  $\mathcal{D}$  is set to the value cited by Sapozhnikov *et al.*

In addition to the calculations of Sapozhnikov *et al.*, similar calculations were also reported by Matula *et al.*<sup>12</sup> for a lithotripsy bubble. For the case simulated, their model predicts that about an order of magnitude more gas molecules will diffuse into the bubble than does the present model. Although vapor transport is included in these model calculations, it affects the diffusion of non-condensable gases very little; hence, the model presented by Matula *et al.* is also expected to predict much more gas diffusion than the model from Sapozhnikov *et al.* For the bubbles studied by Sapozhnikov *et al.*, such a high level of diffusion would lead to bubble dissolution times that are 5–10 times longer than were observed. Rather than the zeroth-order Eller-Flynn solution used here, Matula *et al.* adopted the modeling approach presented by Fyrrillas and Szeri,<sup>36</sup> which should be more accurate. However, they do not discuss implementation details for the type of transient motion that characterizes lithotripsy bubbles. Ultimately, we consider the calculations presented by Sapozhnikov *et al.* as the relevant benchmark because these

calculations were consistent with experimental observations that directly reflect gas diffusion. The higher transient diffusion rates predicted by Matula *et al.* could be consistent with these observations if each lithotripsy bubble broke into many daughter bubbles. However, even if the experimental lithotripsy bubbles did break into numerous daughter bubbles, it is unclear that the subsequent dissolution of closely spaced bubbles would proceed quickly enough and consistently enough to match the observed dissolution times.

Aside from modeling gas diffusion, the same convolution solution was used in the PZ model to calculate heat diffusion in the liquid. The transient, monotonic growth of vapor bubbles in superheated water has been studied theoretically and experimentally, thereby providing data for comparison. As noted by Plesset and Zwick,<sup>52</sup> such growth can be split into two regimes. Rapid initial growth is controlled by surface tension and the inertia of the surrounding liquid; subsequent slower growth is limited by the thermal conduction of heat from the surroundings to the bubble. Plesset and Zwick developed an asymptotic model for the thermally controlled regime and found their model to closely match experimental observations. As the bubble grows relatively large, this model predicts the bubble radius to be proportional to the square root of time; such calculations are compared to predictions from the SCL and PZ models in Fig. 6(a). First, note the dashed lines at left that represent the SCL model at 102 °C and 106 °C. Because the SCL model employs an instantaneous algebraic solution for heat diffusion in the liquid, it cannot capture the evolution of a thermal boundary

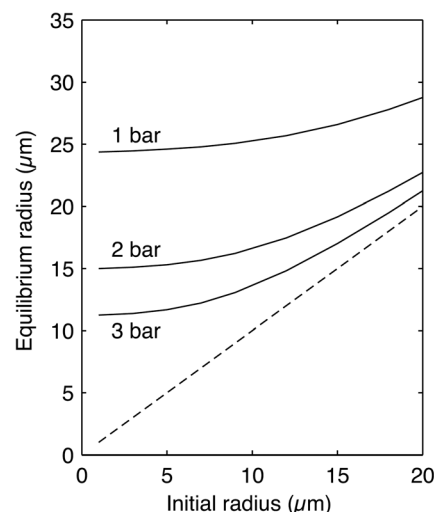


FIG. 5. Calculations of the transient diffusion of dissolved gases into a bubble excited by a lithotripter shock wave. For each indicated static pressure in the liquid, bubble oscillation and the concomitant diffusion lead to a new equilibrium bubble radius for a given initial radius. The dashed line denotes the locus of points corresponding to zero net diffusion such that initial and equilibrium radii are the same. The plot was generated for comparison with Fig. 3 from Sapozhnikov *et al.*<sup>11</sup> and shows virtually the same results. Calculations utilized the SCL model, neglected vapor transport, assumed an ambient temperature of 20 °C, and assumed an initial concentration of dissolved gases corresponding to equilibrium at a pressure of 1 bar. The lithotripter shock wave was modeled by assuming an instantaneous pressure rise to the shock's peak positive value  $p_{sw}$  at time  $t=0$ . Following Sapozhnikov *et al.*, subsequent acoustic pressures were modeled as  $2p_{sw}e^{-\alpha t} \cos(2\pi ft + \pi/3)$ , where  $p_{sw} = 50$  MPa,  $\alpha = 9.1 \times 10^5$  s<sup>-1</sup>, and  $f = 83.3$  kHz.

layer that limits heat conduction and the bubble's growth rate. In contrast, relative agreement between the PZ model (solid lines) and Plesset and Zwick's asymptotic solution (dotted lines) demonstrates that the convolution does capture transient thermal effects. At both 102 °C and 106 °C, the PZ model predicts slightly higher growth rates than the asymptotic model, suggesting that it underestimates the effective boundary-layer thickness and overestimates the ability of heat to flow between the distant surroundings and the bubble.

For an additional benchmark pertinent to heat diffusion, we also consider the vapor-bubble model presented by Hao and Prosperetti.<sup>53</sup> For a vapor bubble in water at 100 °C, they simulate the response of a 35  $\mu\text{m}$  bubble to a 1 kHz, 0.4 atm sine wave. Their calculations predict rectified heat transfer leading to bubble growth up to and beyond the resonance radius. As shown in Fig. 6(b), the PZ model demonstrates the same qualitative behavior, while the SCL does not. Note that the dotted lines in this figure represent the envelope of the radius-time curve reported by Hao and Prosperetti. Because the SCL model does not capture the evolution of a thermal boundary layer, heat is readily conducted to/from the surroundings and the bubble cannot concentrate energy to grow by rectified heat transfer. In contrast, the PZ model does predict rectified heat transfer and bubble growth through resonance. Notably, the PZ model predicts slightly slower bubble growth than the Hao and Prosperetti model, both before and after resonance size is reached. Moreover, after the bubble grows beyond resonance size, the PZ model predicts larger peak-to-peak oscillations during each acoustic cycle. Because the oscillatory stiffness of vapor bubbles depends upon the concentration of thermal effects in the liquid close to the bubble, larger oscillations coupled with slower overall growth rates are consistent with the earlier observation that the PZ model slightly overestimates the instantaneous rate of heat transfer between the bubble and the distant surroundings.

Convolution calculations in the present model rely on a basic assumption that diffusion is slow and the diffusive boundary layer remains thin. As discussed by Fyrrillas and Szeri,<sup>36</sup> the assumption of a thin boundary layer is tantamount to the presence of a large Peclet number, which is inversely proportional to the diffusivity. Given that the thermal diffusivity of water is about 70 times larger than the diffusivity of dissolved air in water, we would expect this thin-boundary-layer assumption to be more restrictive for heat diffusion. In addition, we note that the model implementation utilizes integration substeps to treat transient bubble motions for which the radial bubble dynamics are not necessarily decoupled from diffusion. In this context, the calculations shown in Figs. 5 and 6 provide useful benchmarks of overall model performance and demonstrate that the present model appears to capture the basic features of transport behavior. Because the zeroth-order convolution tends to underestimate the boundary-layer thickness, net transport is overestimated during any monotonic bubble growth or collapse. However, for an oscillating bubble, the thinner boundary layer implies that the bubble is more closely coupled to the surrounding liquid as a source or sink; as such, "concentrating" behaviors like rectified diffusion and rectified heat transfer will be less prevalent.

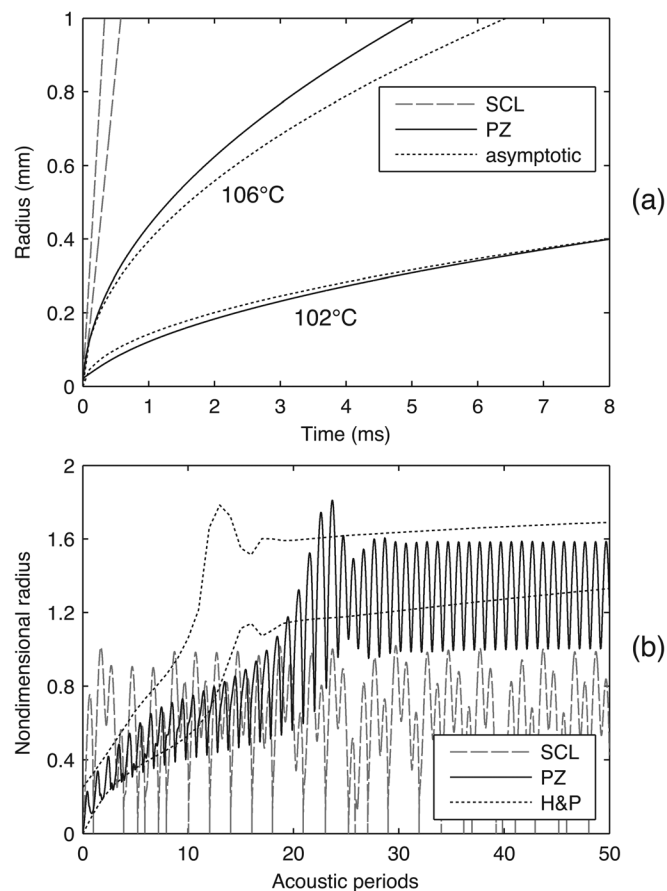


FIG. 6. Calculations to benchmark model performance for vapor bubbles, whereby bubble motion is coupled to thermal conduction in the surrounding liquid. (a) The radial growth of superheated vapor bubbles is plotted for the surrounding liquid at two initial temperatures. PZ and SCL model calculations are compared with the asymptotic approximation derived by Plesset and Zwick.<sup>52</sup> Note that the initial bubble growth rate is influenced primarily by the initial radius (assumed to be 20  $\mu\text{m}$  here) rather than thermal conduction in the liquid; accordingly, this rate is not a part of the asymptotic approximation. With regard to the ultimate growth rates, the PZ model predicts slightly faster growth while the SCL model predicts much faster growth. Identical fluid properties are used for calculations from the present models and the asymptotic approximation. (b) Calculations of rectified heat transfer are plotted for a 35  $\mu\text{m}$  bubble in 100 °C water after excitation by a 0.4 atm sine wave at 1 kHz. Note that the plotted bubble radius is normalized relative to the resonance size of 2.71 mm for a vapor bubble. The plot includes lines for the PZ and SCL models as well as an envelope that represents the results reported in Fig. 3 from Hao and Prosperetti (H&P).<sup>53</sup>

### 3. Simulation of violent bubble collapses

With regard to violently collapsing bubbles, single-bubble sonoluminescence is a phenomenon that has been studied in detail. In particular, Storey and Szeri<sup>17</sup> have reported model calculations to elucidate the physical mechanisms that affect the collapse dynamics of individual sonoluminescence bubbles. For comparison with the present model, the "case II" calculations of Storey and Szeri are considered here, allowing for vapor transport in the absence of chemical reactions or mass diffusion in the liquid. This case pertains to the response of a 4.5  $\mu\text{m}$  bubble excited by a sinusoidal pressure wave of 1.2 bar at 26.5 kHz. Their simulations consider an argon bubble in water at 25 °C; for comparison, the air bubble described by the present model is treated using the fluid properties described in Sec. 3.3, with the thermal conductivity of

air multiplied by  $2/3$  to approximate that of argon.<sup>54</sup> This implementation of the fluid properties is very similar to that used by Storey and Szeri; a notable difference is their use of a non-ideal equation of state inside the bubble.

For benchmarking purposes, the bubble's energy content before, during, and after a violent collapse are of interest. First, we compare radius-time curves, as shown in Fig. 7(a). In this plot, the solid line represents calculations from the present PZ model, while the dotted lines mark peak radii reported by Storey and Szeri between collapses. While the PZ model predicts a maximum radius that is about 3% smaller, subsequent peak radii decay more quickly with the PZ model to imply higher damping. This increased damping is consistent with the earlier conclusion that the PZ model tends to overestimate the exchange of heat with the surroundings, which act here as a sink that dissipates heat generated during each collapse. In addition to the smaller maximum radius, we also note that the minimum radius of  $0.38 \mu\text{m}$  is less than the  $0.70 \mu\text{m}$  value reported by Storey and Szeri. Discrepancies in absolute values of bubble radius are expected given the use of different equations of state in the gas as well as the consideration of spatial inhomogeneities by Storey and Szeri. Accordingly, it is useful to assess energy concentration inside the bubble by the peak gas temperature rather than the minimum bubble radius. Along these lines, the PZ model predicts a peak temperature of 4200 K throughout the bubble, while Storey and Szeri predict a peak of 9700 K at the center. Because the PZ model assumes spatial homogeneity, the 4200 K prediction represents a spatial average, which should clearly be lower than the spatial peak. These peak temperatures are consistent with one another.

A main point made by Storey and Szeri as well as by Toegel *et al.*<sup>35</sup> is that peak temperatures are affected by the trapping of vapor molecules inside the bubble during late stages of collapse. As shown in Fig. 7(b), the PZ model predicts that the molar fraction of vapor at the end of the initial collapse is 7%, whereas Storey and Szeri report 14%. In this plot, the dotted lines again denote the peak values predicted by Storey and Szeri between collapses. Because both models predict the same maximum value prior to the initial collapse, we conclude that the PZ model predicts less influence of diffusion inside the bubble as far as limiting the rate of condensation during collapse. Such a discrepancy is not surprising since the PZ model does not attempt to simulate full details of the gas dynamics. Nonetheless, the PZ model appears to capture the basic vapor-trapping behavior.

Another aspect of the model that is closely coupled to phase change at the bubble wall is the liquid temperature at this interface. Figure 7(c) shows this temperature as calculated by the SCL and PZ models. The dotted horizontal line denotes the critical temperature of water, and the open circles indicate the times between which the temperature exceeds the critical value in Storey and Szeri's calculations. First, we note that the temperature for the SCL model is almost symmetric about the time of the bubble's minimum radius. This result is easily explained in that the interface temperature is algebraically calculated at each instant and is essentially determined by the state of compression of the gas inside the bubble. In contrast, the other two models display

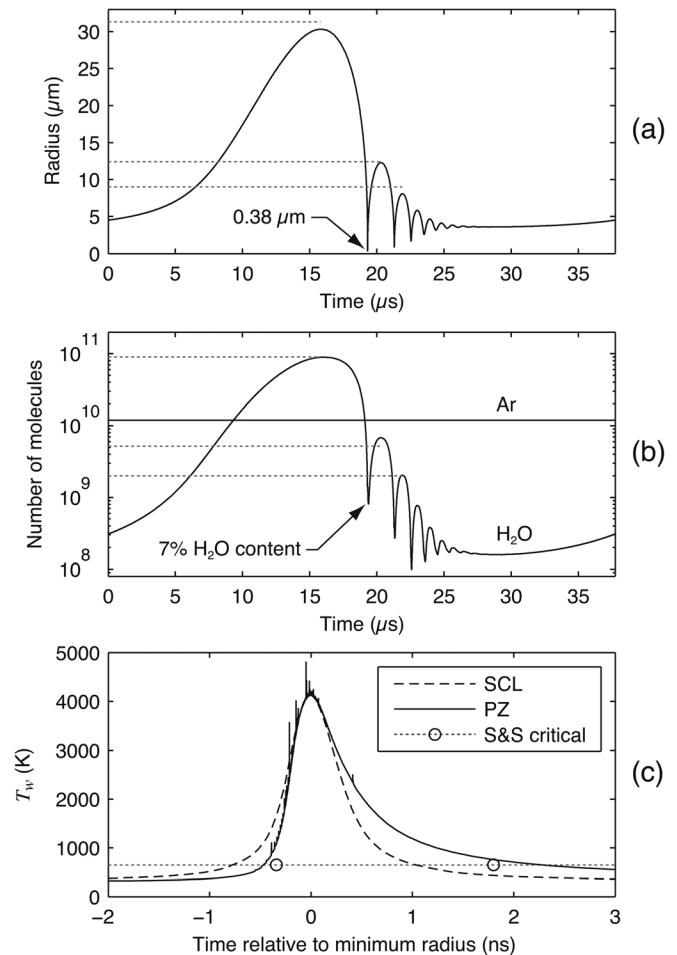


FIG. 7. Model calculations for comparison with the “case II” sonoluminescence bubble described by Storey and Szeri.<sup>17</sup> In this case, a  $4.5 \mu\text{m}$  bubble is harmonically excited with a pressure amplitude of 1.2 bar at 26.5 kHz. Simulations consider an air bubble in water at 298 K; for comparison with Storey and Szeri’s calculations, diffusion of non-condensable gases is neglected and the thermal conductivity of air is multiplied by  $2/3$  to approximate that of argon.<sup>54</sup> (a) The radius-time curve predicted by the PZ model is plotted, with the horizontal dotted lines marking specific peak radii reported by Storey and Szeri. (b) Solid lines represent PZ model calculations for bubble contents in terms of argon and water vapor; horizontal dotted lines indicate peak numbers of vapor molecules reported by Storey and Szeri. (c) Liquid temperatures at the bubble wall are plotted for the SCL and PZ models, showing that the choice of  $A_T = 1.3$  in the SCL model matches the PZ model’s peak temperature. The noise in PZ model calculations reflects a numerical instability at small time steps, as discussed in Sec. 3.2. Last, the dotted line denotes the critical temperature of water, while the open circles mark the times between which Storey and Szeri reported supercritical temperatures.

an asymmetry in the temperature, owing to the buildup of heat throughout the collapse. As such, the history of the bubble motion affects the temperature at any given time. While both the PZ model and the calculations from Storey and Szeri exhibit similar asymmetries, it is interesting that the PZ model predicts supercritical temperatures for a slightly longer duration. Given the previous discussion that the PZ convolution overestimates thermal conduction between the bubble and the surroundings in the liquid phase, we might expect the opposite result. However, the interface temperature during a violent collapse is controlled not only by thermal conduction in the liquid, but also by thermal conduction in the gas phase (which acts as a boundary condition for

thermal diffusion in the liquid). Hence, the longer duration of supercritical temperatures suggests that thermal conduction in the gas is overestimated. Since thermal conduction is calculated from Eqs. (18) and (19), we conclude that the boundary layer thickness in the gas is underestimated. Although the tuning defined by  $A_\theta = 0.5$  matches thicknesses reported by Preston for a bubble containing an ideal gas,<sup>18</sup> the prediction of a smaller minimum radius of 0.38  $\mu\text{m}$  for the present case apparently distorts the spatial scaling for thermal conduction. Based on all of the comparisons in Fig. 7, the bubble contents and associated peak temperatures predicted by the PZ model are generally consistent with the more detailed calculations of Storey and Szeri. We conclude that the PZ model provides a realistic estimate of the bubble's energy even during the late stages of a violent collapse. Accordingly, the model should provide a reasonable approximation of the energy dissipated during a violent collapse.

Additional benchmarks regarding energy dissipation can be determined by comparison with calculations reported by Matsumoto *et al.*<sup>15</sup> Exploring the use of bubbles to transduce incident acoustic energy into heat for thermal therapies such as HIFU, they considered energy deposition to the surrounding medium via three mechanisms: viscous damping, thermal conduction, and acoustic radiation. For air bubbles, they report radial responses and rates of energy deposition for a range of initial bubble sizes. The PZ model was used to simulate the same conditions in ambient water at 20 °C, where bubbles are excited by a 100 kPa sine wave at 1 MHz. In Fig. 8(a), resonance curves are compared. While the present model predicts a curve with the same shape as reported by Matsumoto *et al.*, it predicts the bubble to undergo smaller oscillation amplitudes. This result is consistent with the above comparison to Storey and Szeri's calculations for a sonoluminescence bubble, where the PZ model predicted a smaller maximum radius. In Fig. 8(b), energy deposition mechanisms associated with bubble motions are illustrated; plotted lines reflect PZ model calculations, and the open circles represent thermal conduction calculations reported by Matsumoto *et al.* Because energy deposition by viscous dissipation and acoustic radiation is virtually the same for both models, the corresponding calculations from Matsumoto *et al.* are not shown in Fig. 8(b). However, the plot highlights that significantly higher thermal damping is predicted by the PZ model for bubbles near resonance. Notably, higher thermal conduction in the gas for the PZ model was also inferred in the previous benchmark for a sonoluminescence bubble. Again, we attribute the discrepancy to gas dynamics that are more complicated than those captured by the present reduced-order model. Although the discrepancy in thermal conduction is significant for a resonant bubble at the relatively low excitation amplitude of 100 kPa, acoustic radiation quickly becomes the dominant damping mechanism at higher acoustic pressures. Moreover, acoustic radiation is captured well by the present models.

## V. RESULTS

Using the tuned model, numerical results were generated for conditions pertinent to therapeutic ultrasound, with

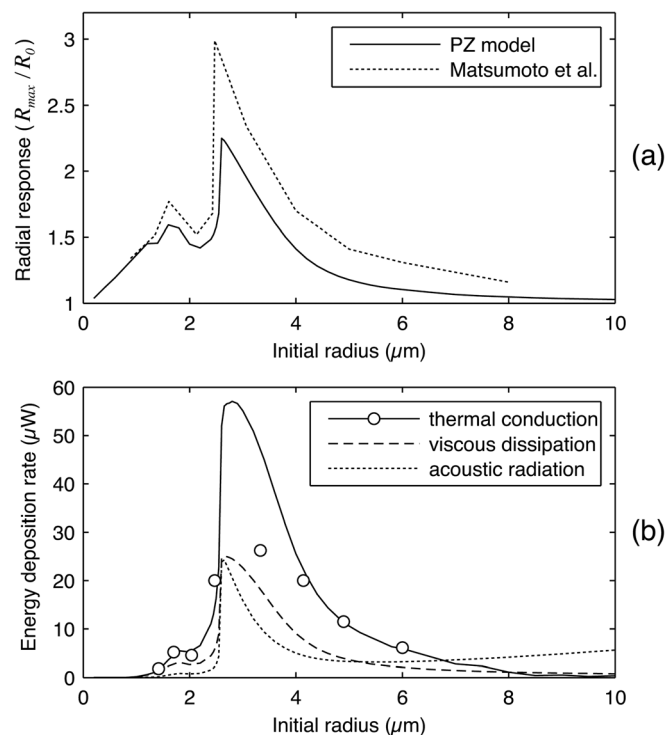


FIG. 8. Comparison of energy dissipation between the PZ model and calculations reported by Matsumoto *et al.*<sup>15</sup> for bubbles excited by a 100 kPa sine wave at 1 MHz. Calculations represent air bubbles in water at 20 °C. (a) Resonance curves demonstrate that the PZ model predicts lower oscillation amplitudes. (b) Energy deposition rates predicted by the PZ model are compared for thermal conduction, viscous dissipation, and acoustic radiation. Matsumoto *et al.* report essentially the same dissipation rates for viscous and acoustic mechanisms; however, for resonant bubbles, they predict about half of the energy deposition rate by thermal conduction, as represented by the open circles.

a particular focus on behaviors at elevated temperatures. First, calculations identifying the resonance structure of gas-vapor bubbles are presented. Next, the dynamics of HIFU bubbles are investigated to explore energy deposition related to inertial bubble collapses.

### A. Bubble resonances

A basic aspect of any dynamic system is its resonance structure. Bubbles containing non-condensable gases can easily be described as a single-degree-of-freedom system in which the surrounding liquid provides an effective mass and the gas pressure inside the bubble represents a spring-like stiffness. The undamped resonance frequency (in hertz) of a gas bubble is described by the following expression:<sup>32</sup>

$$f_g = \frac{1}{2\pi} \sqrt{\frac{3\gamma(p_0 + 2\sigma/R_0) - 2\sigma/R_0}{\rho R_0^2}} \quad (29)$$

The symbols used here have the same meanings as in the earlier modeling section:  $\gamma$  is the ratio of specific heats in the gas,  $\sigma$  is surface tension,  $p_0$  is the static pressure in the liquid, and  $R_0$  is the undisturbed bubble radius. Because vapor can condense, vapor bubbles possess a different stiffness than gas bubbles. Rather than arising from the compression of non-condensable gases, the stiffness of a vapor bubble comes from

thermal behaviors.<sup>53</sup> As a bubble collapses, vapor condenses and heats the surrounding liquid, which in turn raises the saturation pressure of the vapor inside the bubble. As described by Hao and Prosperetti,<sup>53</sup> vapor bubbles can exhibit two resonance-like behaviors: a true resonance for which the thermal stiffness is balanced by inertial forces and an unstable pseudo-resonance for which the thermal stiffness is balanced by surface tension. Hao and Prosperetti present the following approximate expressions for stable and unstable resonance frequencies of vapor bubbles:

$$f_{vs} = \frac{1}{2\pi} \left[ \frac{0.56 \mathcal{L}^4 \rho_m^4}{R_0^2 \rho_0^3 c_{pl} k_\ell T_\infty^2} \right]^{1/3} \quad (30)$$

$$f_{vu} = \frac{1}{2\pi} \frac{0.94}{R_0^4} \frac{k_\ell}{\rho_0 c_{pl}} \left[ \frac{2\sigma c_{pl} \rho_0 T_\infty}{(\mathcal{L} \rho_m)^2} \right]^2. \quad (31)$$

Because our interest here is in gas-vapor bubbles, we seek to plot these three expressions together for gas and vapor bubbles, while using the present model to explore the resonances of gas-vapor bubbles.

For air bubbles in water at  $T_\infty = 100^\circ\text{C}$ , resonances were determined numerically from the PZ model by sweeping the initial bubble radius for excitations at a given frequency. For gas-vapor bubbles, the bubble was initialized such that its partial pressure of vapor was equal to the saturation pressure at  $T_\infty$ . Peaks in the amplitude of the response  $\Delta R/R_{eq}$  were identified as resonances, where  $R_{eq}$  is the equilibrium radius about which oscillations occur, and  $\Delta R$  is the amplitude of these oscillations. Notably, the resonance frequencies of both gas and vapor bubbles can be affected by the amplitude of the excitation<sup>53,55</sup>; accordingly, resonances were identified by using the lowest excitation amplitudes that were able to produce steady-state (or nearly steady-state) oscillations. In Fig. 9, the solid and dashed lines represent resonance frequencies calculated from Eqs. (29)–(31), while the individual marks represent resonances identified numerically from the PZ model. Of the dashed lines corresponding to vapor-bubble resonances, the more vertical line

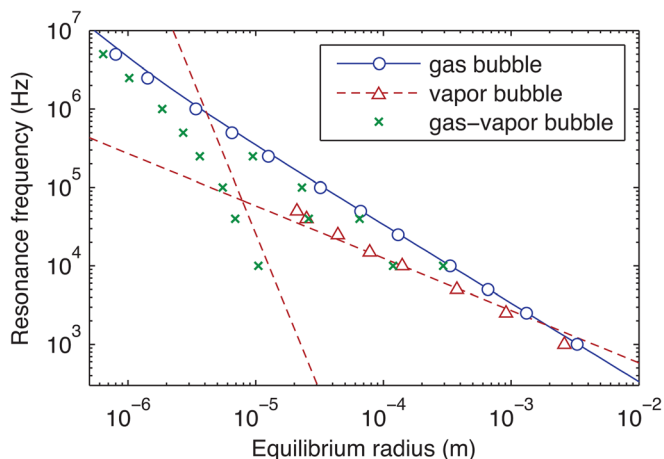


FIG. 9. (Color online) Resonances of gas bubbles, vapor bubbles, and gas-vapor bubbles. All resonances assume an air bubble in water at  $100^\circ\text{C}$ . Solid and dashed lines represent analytical expressions, while the discrete marks represent peaks in the response predicted by the PZ model.

represents unstable pseudo-resonances. To the left of this line, surface tension is dominant and no stable motions of vapor bubbles are possible.

In Fig. 9, it is clear that the PZ model exhibits resonance behaviors that match analytical predictions for gas bubbles and for stable resonances of vapor bubbles. Because pseudo-resonances are by definition unstable, these resonances were not able to be identified numerically from the PZ model. For gas bubbles, we note that the analytical resonance frequencies at any given radius are slightly higher than those from the PZ model, especially for smaller bubbles. This discrepancy is explained by the inclusion of viscous and thermal damping in the PZ model [such damping is omitted from the analytical expression (29)]. For vapor bubbles larger than about 0.5 mm, the PZ model predicts lower resonance frequencies than Eq. (30); for smaller bubbles, the PZ model predicts higher frequencies. This trend is fully consistent with calculations presented by Hao and Prosperetti that utilize a more complete formulation than is captured by Eq. (30). Last, we note that the resonances identified for gas-vapor bubbles correspond to both gas and vapor resonances. Moreover, because the presence of non-condensable gas stabilizes very small bubbles, resonances can be identified near the pseudo-resonance line. Interestingly, at 10 and 40 kHz, three distinct resonance sizes were found, matching the three analytical resonances. For gas-vapor bubbles at micron sizes that can be relevant in therapeutic ultrasound, the added thermal effects of vapor appear to lower the effective resonance frequencies relative to those for gas bubbles.

## B. HIFU bubbles

HIFU treatments typically involve rapid heating in conjunction with the potential for violent cavitation activity.<sup>56</sup> Gaining insight into the bubble dynamics under such conditions requires an understanding of heat and mass transport for bubbles excited by high acoustic pressures at elevated temperatures. Under these conditions, it is necessary to account for vapor transport; a particular challenge for such models is maintaining numerical stability through violent bubble collapses. Accordingly, the present model has utility in simulating the relevant bubble dynamics.

A specific area of interest involves the potential for bubble activity to enhance the rate of HIFU heating.<sup>13,56–58</sup> As described initially by Holt and Roy<sup>13</sup> (and illustrated in Fig. 8), oscillating bubbles can deposit energy in the surrounding medium by thermal conduction, viscous dissipation, or acoustic radiation. While some HIFU applications use ultrasound contrast agents in conjunction with relatively low excitation pressures around 1 bar,<sup>15,57</sup> we focus here on treatments that involve excitation pressures on the order of megapascals. Bubbles excited at such pressures deposit energy primarily by acoustic radiation as they inertially collapse and emit short acoustic pulses that have broadband frequency content. In this way, HIFU bubbles transduce the incident acoustic wave at megahertz frequencies to waves that contain energy at much higher frequencies. Because acoustic absorption increases with frequency, this transduction enhances the rate of heating within the focal region of the HIFU treatment.

To explore how thermodynamic conditions relevant to HIFU affect the bubble dynamics and the potential for bubble-enhanced heating, the PZ model was used to simulate the response of a  $2\ \mu\text{m}$  bubble to a sinusoidal excitation at 2 MHz and 2 MPa. To account for changing temperature conditions during a HIFU treatment, simulations were performed for ambient temperatures ranging from  $T_\infty = 20^\circ\text{C}$  to  $95^\circ\text{C}$ . Bubble responses were simulated over 250 acoustic cycles to capture the behavior after any start-up transients. Samples of the predicted radial dynamics are plotted in Fig. 10(a). At  $20^\circ\text{C}$ , the bubble grows to a maximum radius of about  $12\ \mu\text{m}$  and collapses inertially every second or third cycle. At  $95^\circ\text{C}$ , the bubble growth is more pronounced (maximum radius over  $20\ \mu\text{m}$ ) and the collapses are much less frequent. Also, we note that the minimum radius obtained during collapse is smaller at  $20^\circ\text{C}$ .

The broadband energy acoustically radiated from the bubble was calculated based on the pressure at the bubble wall as defined by Eq. (10). Across a range of temperatures, the energy spectral density of the pressure signal was averaged between 10 and 50 MHz and normalized relative to the energy spectral density at 2 MHz of the excitation pressure waveform. Note that the energy spectral density is proportional to the magnitude squared of the Fourier transform of

the signal. This metric of broadband acoustic radiation is plotted for the PZ model in Fig. 10(b), showing a steep decline as temperature increases. Because broadband acoustic radiation is the dominant dissipation mechanism for this bubble, this plot implies that the potential for bubbles to enhance heating during HIFU will decrease quickly as temperatures rise above about  $60^\circ\text{C}$ . Between  $60^\circ\text{C}$  and  $80^\circ\text{C}$ , the PZ model predicts a decline in broadband energy by more than 2 orders of magnitude. To better understand the role of vapor in causing this sensitivity to  $T_\infty$ , calculations were repeated for two model variations: the SCL model and a “static vapor” model in which explicit vapor transport is neglected. As proposed by Wu,<sup>59</sup> the latter model accounts for temperature changes by reducing the static liquid pressure from  $p_0$  to  $p_0 - p_{\text{sat}}$ , where  $p_{\text{sat}}$  is evaluated at  $T_\infty$ . Results of these calculations are also shown in Fig. 10(b). Clearly, the “static vapor” model misses the quenching effect predicted by the PZ model. On the other hand, the SCL model predicts a quenching effect that is somewhat less severe than that from the PZ model. Interestingly, the SCL model predicts less broadband radiation than the PZ model even at  $20^\circ\text{C}$ . An explanation for this result relies on the prior conclusion that the SCL model conducts thermal energy between the bubble and the surroundings more easily than the PZ model. Accordingly, the SCL model predicts more thermal damping so that inertial collapses are on average less violent and less energy is dissipated by acoustic radiation.

The previous calculations pertain to a specifically sized bubble excited by a pressure waveform at a particular amplitude and frequency. However, HIFU treatments may involve a wide range of excitation frequencies, amplitudes, and bubble sizes. Although a comprehensive investigation of such a parameter space is beyond the scope of this effort, the role of temperature and vapor across a range of bubble collapses can be explored relatively easily. Neglecting the compressive part of a HIFU waveform that forces bubble collapse, we consider Rayleigh collapses characterized by different maximum radii and ambient temperatures. With this approach, the maximum radius prior to collapse serves as a proxy measure for the initial bubble size as well as the excitation amplitude and frequency. To simulate this range of collapses, a series of half-cycle sinusoids was considered as excitations for a  $1\ \mu\text{m}$  bubble. The sinusoids were defined as  $-A \sin(2\pi ft)$ . Accordingly, the half-cycle excitations comprised a single negative pulse that forced bubble growth. To achieve a maximum radius  $R_{\text{max}}$  and a subsequent free collapse, we set  $A = 3.75\ \text{MPa}$  and defined the frequency  $f$  so that the period was one-fifth of the Rayleigh collapse time associated with  $R_{\text{max}}$  (i.e.,  $5(1/f) = 0.915R_{\text{max}}\sqrt{\rho_0/\rho_0}$ ). This approach was used to simulate bubble collapses as a function of both  $R_{\text{max}}$  and  $T_\infty$ .

To summarize the results from 464 simulated collapses, the energies dissipated by acoustic radiation during each collapse are represented by the contour plot in Fig. 11. For comparison among differently sized bubbles, the plotted energies were normalized relative to an energy associated with the bubble’s size:  $(4/3)\pi R_{\text{max}}^3 \rho_0 + 4\pi R_{\text{max}}^2 \sigma$ . Accordingly, the contours identify bubble sizes and temperatures for which unforced collapses have the same efficiency in converting available energy into acoustic radiation. For  $R_{\text{max}}$  less than

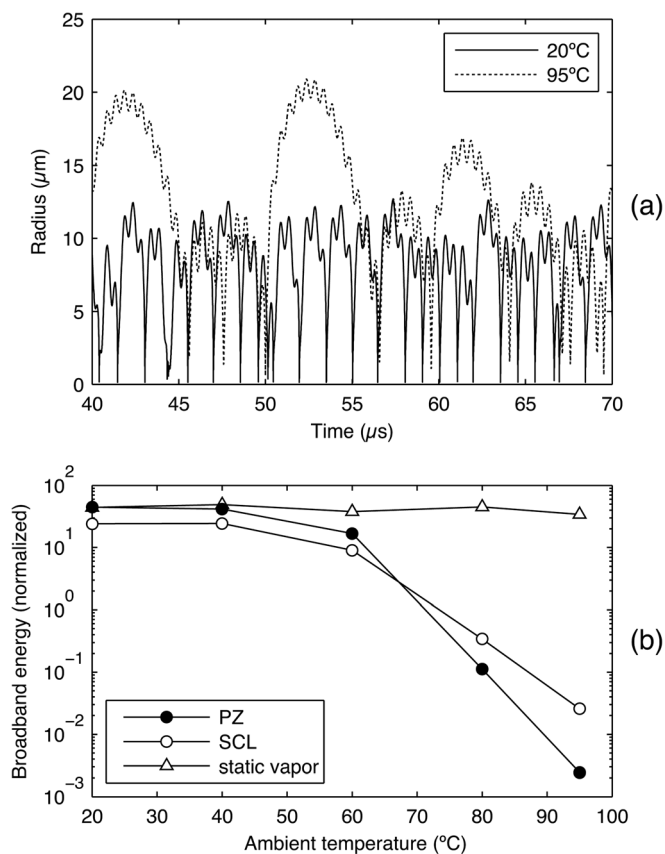


FIG. 10. Model simulations for a  $2\ \mu\text{m}$  bubble excited by a 2 MPa sinusoidal HIFU waveform at 2 MHz. (a) Examples of the predicted radial dynamics at low and high temperatures. (b) Variation of the broadband acoustic energy radiated by the bubble as a function of the ambient temperature and the bubble model used for the simulation. The “static vapor” model simulates a bubble with only non-condensable gas, while reducing the static liquid pressure by the saturation vapor pressure at a given ambient temperature.

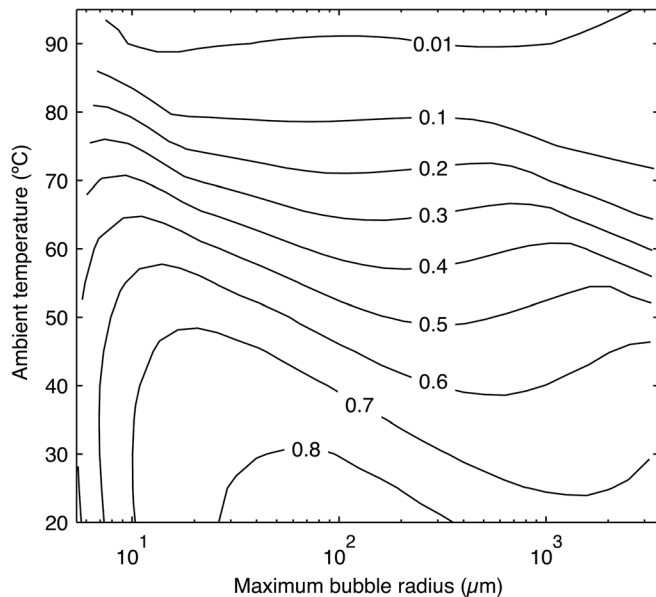


FIG. 11. Contour plot showing the efficiency with which forced bubble collapses convert energy into outgoing pressure waves. The maximum bubble radius prior to collapse serves as a proxy for HIFU excitation conditions, while the role of vapor is explored by varying the temperature of the ambient liquid. Bubble calculations were performed using the PZ model for air bubbles in gas-saturated water. In simulations, bubbles were excited by a short, negative pressure pulse described by a half cycle of a sine wave. Bubbles underwent a primary growth, an unforced collapse, and a subsequent rebound. To account for the variation in available energy with bubble size, acoustically radiated energies calculated from each collapse were normalized relative to an energy defined by the bubble's volume and surface area.

about  $10 \mu\text{m}$ , the contours tend to have a positive slope because larger bubbles possess more inertia to drive more violent collapses. However, as  $R_{\text{max}}$  continues to increase, the contours tend to have a negative slope. This trend is caused by vapor trapping, whereby the extra vapor molecules present prior to the collapse of larger bubbles cannot condense quickly enough to prevent a “cushioning” effect. As  $R_{\text{max}}$  increases further, the contour slope changes to become positive again. This transition happens more quickly at elevated temperatures and is indicative of a transition to thermally controlled collapses for which vapor trapping is no longer important.

## VI. DISCUSSION AND CONCLUSIONS

A reduced-order approach for modeling the dynamics of a bubble excited by therapeutic ultrasound is presented. Because relevant conditions for such bubbles include high excitation pressures and elevated temperatures, the model includes heat transport in the gaseous and liquid phases as well as the transport of vapor and non-condensable gases. As a part of the modeling approach, two methods for calculating the temperature in the liquid at the bubble wall are proposed: The SCL model calculates this temperature algebraically by assuming a temperature gradient based on a scaling of the problem. In contrast, the PZ model does not require scaling assumptions but rather uses a convolution as a low-order approximate solution for the diffusive transport. The two models are complementary in that the SCL model is utilized to enhance the numerical stability of the more complete PZ model.

The PZ and SCL models possess two free parameters related to mass diffusion inside the bubble, which can limit the rate of condensation at the bubble wall. These two parameters were tuned using experimental observations of the collapses and rebounds of lithotripsy bubbles under varying conditions. By tuning these parameters, the PZ model is able to successfully fit experimental observations under 8 separate test conditions, while the SCL model provides successful fits only at lower temperatures. The tuned PZ model was then benchmarked against results from other models in the literature. Benchmark results demonstrate that the model is capable of capturing behaviors such as rectified diffusion and rectified heat transfer. Although the basic features of vapor bubble growth due to ambient superheat or rectified heat transfer are captured, these comparisons do suggest that the PZ model underestimates the instantaneous thickness of the thermal boundary layer in the liquid, thereby overestimating the net heat transfer between the bubble and its surroundings. Additional benchmark calculations related to violent bubble collapses demonstrate that the present model provides reasonable predictions, even though more sophisticated models of the gas dynamics inside the bubble yield some quantitative differences.

Ultimately, we conclude that the reduced level of detail of the gas dynamics included in the present model is appropriate for capturing the basic mechanics of violent bubble collapses. In particular, the goal of this model is to elucidate the physics underlying basic trends in bubble behaviors that are likely to be physically realized in experiments and/or treatments. Accordingly, given the sensitivity of bubble-collapse dynamics to various physical uncertainties including the fluid properties or geometric asymmetry,<sup>60</sup> the importance of quantitative discrepancies related to more complicated gas dynamics is diminished. Moreover, Storey and Szeri note that the equation of state used for the gas inside the bubble may affect quantitative predictions, but not the basic physics represented by the model.<sup>17</sup>

An important aspect of the present model is its numerical stability across a broad parameter space. This stability enables a consistent evaluation of the mechanisms underlying trends in bubble behavior. Figure 11 shows such a comparison across a parameter space that includes micron-sized HIFU bubbles with millimeter-sized lithotripsy bubbles. As a result, a model tuned to fit experimental observations of lithotripsy bubbles can be reasonably applied to HIFU bubbles. Based on the calculations presented in Figs. 10 and 11, vapor can strongly alter the collapses of micron-sized HIFU bubbles by cushioning collapses at elevated temperatures. Consequently, treatment strategies that rely on bubble-enhanced heating may be ineffective at temperatures above about  $60^\circ\text{C}$ . Indeed, this prediction appears to be consistent with recent experimental observations of bubble-enhanced heating in a tissue phantom.<sup>61</sup>

## ACKNOWLEDGMENTS

We thank our collaborators at the Center for Industrial and Medical Ultrasound. In particular, we thank Dr. Steven Kargl for helpful suggestions regarding the numerical implementation. This work was supported by the National Institutes

of Health (DK43881, DK070618, EB007643, T32 Bioengineering Cardiovascular Training Grant) and by the National Space Biomedical Research Institute through NASA NCC 9-58.

- <sup>1</sup>S. Qin, C. F. Caskey, and K. W. Ferrara, "Ultrasound contrast microbubbles in imaging and therapy: Physical principles and engineering," *Phys. Med. Biol.* **54**, R27–R57 (2009).
- <sup>2</sup>K. Ferrara, R. Pollard, and M. Borden, "Ultrasound microbubble contrast agents: Fundamentals and application to gene and drug delivery," *Annu. Rev. Biomed. Eng.* **9**, 415–447 (2007).
- <sup>3</sup>Z. Xu, Z. Fan, T. L. Hall, F. Winterroth, J. B. Fowlkes, and C. A. Cain, "Size measurement of tissue debris particles generated from pulsed ultrasound cavitation therapy—histotripsy," *Ultrasound Med. Biol.* **35**, 245–255 (2009).
- <sup>4</sup>S. Bloch, M. Wan, P. Dayton, and K. Ferrara, "Optical observation of lipid- and polymer-shelled ultrasound microbubble contrast agents," *Appl. Phys. Lett.* **84**, 631–633 (2004).
- <sup>5</sup>J.-E. Blatteau, J.-B. Souraud, E. Gempp, and A. Bousuges, "Gas nuclei, their origin, and their role in bubble formation," *Aviat. Space Environ. Med.* **77**, 1068–1076 (2006).
- <sup>6</sup>J. A. McAteer, M. R. Bailey, J. C. Williams, Jr., R. O. Cleveland, and A. P. Evan, "Strategies for improved shock wave lithotripsy," *Ital. J. Urol. Nephrol.* **57**, 271–287 (2005).
- <sup>7</sup>C. F. Caskey, S. M. Stieger, S. Qin, P. A. Dayton, and K. W. Ferrara, "Direct observations of ultrasound microbubble contrast agent interaction with the microvessel wall," *J. Acoust. Soc. Am.* **122**, 1191–1200 (2007).
- <sup>8</sup>J. B. Freund, "Suppression of shocked-bubble expansion due to tissue confinement with application to shock-wave lithotripsy," *J. Acoust. Soc. Am.* **123**, 2867–2874 (2008).
- <sup>9</sup>H. Miao, S. M. Gracowski, and D. Dalecki, "Ultrasonic excitation of a bubble inside a deformable tube: Implications for ultrasonically induced hemorrhage," *J. Acoust. Soc. Am.* **124**, 2374–2384 (2008).
- <sup>10</sup>C. C. Church, "A theoretical study of cavitation generated by an extracorporeal shock wave lithotripter," *J. Acoust. Soc. Am.* **86**, 215–227 (1989).
- <sup>11</sup>O. A. Sapozhnikov, V. A. Khokhlova, M. R. Bailey, J. C. Williams, Jr., J. A. McAteer, R. O. Cleveland, and L. A. Crum, "Effect of overpressure and pulse repetition frequency on cavitation in shock wave lithotripsy," *J. Acoust. Soc. Am.* **112**, 1183–1195 (2002).
- <sup>12</sup>T. J. Matula, P. R. Hilmo, B. D. Storey, and A. J. Szeri, "Radial response of individual bubbles subjected to shock wave lithotripsy pulses *in vitro*," *Phys. Fluids* **14**, 913–921 (2002).
- <sup>13</sup>R. G. Holt and R. A. Roy, "Measurements of bubble-enhanced heating from focused, MHz-frequency ultrasound in a tissue-mimicking material," *Ultrasound Med. Biol.* **27**, 1399–1412 (2001).
- <sup>14</sup>X. Yang, R. Roy, and R. Holt, "Bubble dynamics and size distributions during focused ultrasound insonation," *J. Acoust. Soc. Am.* **116**, 3423–3431 (2004).
- <sup>15</sup>Y. Matsumoto, J. S. Allen, S. Yoshizawa, T. Ikeda, and Y. Kaneko, "Medical ultrasound with microbubbles," *Exp. Therm. Fluid Sci.* **29**, 255–265 (2005).
- <sup>16</sup>V. Q. Vuong and A. J. Szeri, "Sonoluminescence and diffusive transport," *Phys. Fluids* **8**, 2354–2364 (1996).
- <sup>17</sup>B. D. Storey and A. J. Szeri, "Water vapour, sonoluminescence and sonochemistry," *Proc. R. Soc. Lond. A* **456**, 1685–1709 (2000).
- <sup>18</sup>A. T. Preston, "Modeling heat and mass transfer in bubbly cavitating flows and shock waves in cavitating nozzles," Ph.D. thesis, California Institute of Technology, Pasadena, CA, 2004.
- <sup>19</sup>W. Kreider, M. R. Bailey, O. A. Sapozhnikov, and L. A. Crum, "Observations of the collapses and rebounds of millimeter-sized lithotripsy bubbles," *J. Acoust. Soc. Am.*, **130**(5), 3531–3540 (2011).
- <sup>20</sup>Y. T. Didenko and K. S. Suslick, "The energy efficiency of formation of photons, radicals and ions during single-bubble cavitation," *Nature* **418**, 394–397 (2002).
- <sup>21</sup>M. S. Plesset and S. A. Zwick, "A nonsteady heat diffusion problem with spherical symmetry," *J. Appl. Phys.* **23**, 95–98 (1952).
- <sup>22</sup>A. Eller and H. G. Flynn, "Rectified diffusion during nonlinear pulsations of cavitation bubbles," *J. Acoust. Soc. Am.* **37**, 493–503 (1965).
- <sup>23</sup>H. Lin, B. Storey, and A. Szeri, "Inertially driven inhomogeneities in violently collapsing bubbles: The validity of the Rayleigh-Plesset equation," *J. Fluid Mech.* **452**, 145–162 (2002).
- <sup>24</sup>V. A. Akulichev, "Pulsations of cavitation voids," in *High-Intensity Ultrasonic Fields*, edited by L. D. Rozenberg (Plenum Press, New York, 1971), Part IV, pp. 201–259.
- <sup>25</sup>H. G. Flynn, "Cavitation dynamics. I. A mathematical formulation," *J. Acoust. Soc. Am.* **57**, 1379–1396 (1975).
- <sup>26</sup>F. Gilmore, "The growth or collapse of a spherical bubble in a viscous compressible liquid," U.S. Federal Report 26-4, California Institute of Technology, Pasadena, CA, 1952.
- <sup>27</sup>C. Herring, "Theory of the pulsations of the gas bubble produced by an underwater explosion," Technical Report 236, U.S. Office of Scientific Research and Development (1941).
- <sup>28</sup>L. Trilling, "The collapse and rebound of a gas bubble," *J. Appl. Phys.* **23**, 14–17 (1952).
- <sup>29</sup>J. B. Keller and M. Miksis, "Bubble oscillations of large amplitude," *J. Acoust. Soc. Am.* **68**, 628–633 (1980).
- <sup>30</sup>A. Prosperetti and A. Lezzi, "Bubble dynamics in a compressible liquid. Part 1. First-order theory," *J. Fluid Mech.* **168**, 457–478 (1986).
- <sup>31</sup>J. R. MacDonald, "Some simple isothermal equations of state," *Rev. Mod. Phys.* **38**, 669–679 (1966).
- <sup>32</sup>T. G. Leighton, *The Acoustic Bubble* (Academic Press, San Diego, 1994), pp. 67–71, 182–184.
- <sup>33</sup>H. Poritsky, "The collapse or growth of a spherical bubble or cavity in a viscous fluid, in Proceedings of the First U.S. National Congress on Applied Mechanics, edited by E. Sternberg (1952), pp. 813–821.
- <sup>34</sup>A. Prosperetti, L. A. Crum, and K. W. Commander, "Nonlinear bubble dynamics," *J. Acoust. Soc. Am.* **83**, 502–514 (1988).
- <sup>35</sup>R. Toegel, B. Gompf, R. Pecha, and D. Lohse, "Does water vapor prevent upscaling sonoluminescence?," *Phys. Rev. Lett.* **85**, 3165–3168 (2000).
- <sup>36</sup>M. M. Fyrrillas and A. J. Szeri, "Dissolution or growth of soluble spherical oscillating bubbles," *J. Fluid Mech.* **277**, 381–407 (1994).
- <sup>37</sup>V. P. Carey, *Liquid-Vapor Phase-Change Phenomena*, Series in Chemical and Mechanical Engineering (Hemisphere Publishing Corporation, WA, 1992), pp. 112–121.
- <sup>38</sup>I. Akhatov, O. Lindau, A. Topolnikov, R. Mettin, N. Vakhitova, and W. Lauterborn, "Collapse and rebound of a laser-induced cavitation bubble," *Phys. Fluids* **13**, 2805–2819 (2001).
- <sup>39</sup>S. K. Loyalka and J. H. Ferziger, "Model dependence of the temperature slip coefficient," *Phys. Fluids* **11**, 1668–1671 (1968).
- <sup>40</sup>F. Sharipov and D. Kalempa, "Velocity slip and temperature jump coefficients for gaseous mixtures. IV. Temperature jump coefficient," *Int. J. Heat Mass Transf.* **48**, 1076–1083 (2005).
- <sup>41</sup>W. Kreider, "Gas-vapor bubble dynamics in therapeutic ultrasound," Ph.D. thesis, University of Washington, Seattle, WA, 2008.
- <sup>42</sup>J. A. Fay, *Molecular Thermodynamics* (Addison-Wesley, Reading, MA, 1965).
- <sup>43</sup>M. M. van Iersel, J. Cornel, N. E. Benes, and J. T. F. Keurentjes, "Inhibition of nonlinear acoustic cavitation dynamics in liquid CO<sub>2</sub>," *J. Chem. Phys.* **126**, 064508 (2007).
- <sup>44</sup>K. Yasui, "Alternative model of single-bubble sonoluminescence," *Phys. Rev. E* **56**, 6750–6760 (1997).
- <sup>45</sup>Free Software Foundation, Inc., GNU Fortran compiler, available at <http://gcc.gnu.org/fortran/> (Last viewed 6/17/2011).
- <sup>46</sup>J. R. Cash and A. H. Karp, "A variable order Runge-Kutta method for initial-value problems with rapidly varying right-hand sides," *ACM Trans. Math. Softw.* **16**, 201–222 (1990).
- <sup>47</sup>K. Yasui, "Effects of thermal conduction on bubble dynamics near the sonoluminescence threshold," *J. Acoust. Soc. Am.* **98**, 2772–2782 (1995).
- <sup>48</sup>X. M. Yang and C. C. Church, "A model for the dynamics of gas bubbles in soft tissue," *J. Acoust. Soc. Am.* **118**, 3595–3606 (2005).
- <sup>49</sup>A. Vogel and W. Lauterborn, "Acoustic transient generation by laser-produced cavitation bubbles near solid boundaries," *J. Acoust. Soc. Am.* **84**, 719–731 (1988).
- <sup>50</sup>C. C. Church, "Prediction of rectified diffusion during nonlinear bubble pulsations at biomedical frequencies," *J. Acoust. Soc. Am.* **83**, 2210–2217 (1988).
- <sup>51</sup>P. S. Epstein and M. S. Plesset, "On the stability of gas bubbles in liquid-gas solutions," *J. Chem. Phys.* **18**, 1505–1509 (1950).
- <sup>52</sup>M. S. Plesset and S. A. Zwick, "The growth of vapor bubbles in superheated liquids," *J. Appl. Phys.* **25**, 493–500 (1954).
- <sup>53</sup>Y. Hao and A. Prosperetti, "The dynamics of vapor bubbles in acoustic pressure fields," *Phys. Fluids* **11**, 2008–2019 (1999).
- <sup>54</sup>"Thermal conductivity of gases," in *CRC Handbook of Chemistry and Physics*, edited by W. M. Haynes, 91st ed. (CRC Press, Boca Raton, FL, 2011), Chap. 6, pp. 6–184, available at <http://www.hbcpnetbase.com> (date last viewed 6/17/2011).
- <sup>55</sup>A. Prosperetti, "Nonlinear oscillations of gas-bubbles in liquids—steady-state solutions," *J. Acoust. Soc. Am.* **56**, 878–885 (1974).

- <sup>56</sup>C. C. Coussios and R. A. Roy, "Applications of acoustics and cavitation to noninvasive therapy and drug delivery," *Annu. Rev. Fluid Mech.* **40**, 395–420 (2008).
- <sup>57</sup>S. Umemura, K. Kawabata, and K. Sasaki, "In vivo acceleration of ultrasonic tissue heating by microbubble agent," *IEEE Trans. Ultrason. Ferroelectr. Freq. Control* **52**, 1690–1698 (2005).
- <sup>58</sup>C. H. Farny, R. G. Holt, and R. A. Roy, "Temporal and spatial detection of HIFU-induced inertial and hot-vapor cavitation with a diagnostic ultrasound system," *Ultrasound Med. Biol.* **35**, 603–615 (2009).
- <sup>59</sup>T. Wu, "Bubble mediated focused ultrasound: Nucleation, cavitation dynamics, and lesion prediction," Ph.D. thesis, Boston University, Boston, MA, 2007.
- <sup>60</sup>A. Szeri, B. Storey, A. Pearson, and J. Blake, "Heat and mass transfer during the violent collapse of nonspherical bubbles," *Phys. Fluids* **15**, 2576–2586 (2003).
- <sup>61</sup>C. H. Farny, R. G. Holt, and R. A. Roy, "The correlation between bubble-enhanced HIFU heating and cavitation power," *IEEE Trans. Biomed. Eng.* **57**, 175–184 (2010).
- <sup>62</sup>W. Wagner and A. Pruß, "The IAPWS formulation 1995 for the thermodynamic properties of ordinary water substance for general and scientific use," *J. Phys. Chem. Ref. Data* **31**, 387–535 (2002).
- <sup>63</sup>N. Bilaniuk and G. S. K. Wong, "Speed of sound in pure water as a function of temperature," *J. Acoust. Soc. Am.* **93**, 1609–1612 (1993).
- <sup>64</sup>N. Bilaniuk and G. S. K. Wong, "Erratum: Speed of sound in pure water as a function of temperature," *J. Acoust. Soc. Am.* **99**, 3257 (1996).
- <sup>65</sup>E. S. Domalski and E. D. Hearing, "Condensed phase heat capacity data," *NIST Chemistry WebBook, NIST Standard Reference Database Number 69*, edited by P. J. Linstrom and W. G. Mallard, (National Institute of Standards and Technology, Gaithersburg MD, 2005), available online <http://webbook.nist.gov> (Last viewed 6/17/2011).
- <sup>66</sup>D. F. Othmer and M. S. Thakar, "Correlating diffusion coefficient in liquids," *Ind. Eng. Chem.* **45**, 589–593 (1953).
- <sup>67</sup>J. Kestin and J. H. Whitelaw, "Sixth international conference on the properties of steam—transport properties of water substance," *J. Eng. Power Trans. ASME* **88**, 82–104 (1966).
- <sup>68</sup>J. Kestin, J. V. Sengers, B. Kamgar-Parsi, and J. M. H. Levelt Sengers, "Thermophysical properties of fluid H<sub>2</sub>O," *J. Phys. Chem. Ref. Data* **13**, 175–183 (1984).
- <sup>69</sup>R. Battino, T. R. Rettich, and T. Tominaga, "The solubility of nitrogen and air in liquids," *J. Phys. Chem. Ref. Data* **13**, 563–600 (1984).
- <sup>70</sup>J. O. Hirschfelder, C. F. Curtiss, and R. B. Bird, *Molecular Theory of Gases and Liquids* (John Wiley and Sons, New York, 1954), pp. 646–648.
- <sup>71</sup>P. M. Silverberg and L. A. Wenzel, "The variation of latent heat with temperature," *J. Chem. Eng. Data* **10**, 363–366 (1965).